

University of Groningen
Quantum Interactions and Structural Dynamics,
Zernike Institute for Advanced Materials

Master Thesis:
Absolute cross section measurements of ions on coronene

Author:

Mart Johan Deuzeman
1683527

Supervisors:

Drs. Geert Reitsma
Dr. Thomas Schlathölter
Prof. dr. ir. Ronnie Hoekstra

Referee:

Dr. Steven Hoekstra

July 2, 2014

Abstract

In this thesis, a method for obtaining absolute cross sections of interactions of ions with molecules, leading to loss of the molecules, is tested. The great asset of this method is that it can be used for molecules for which it is hard to produce a dense target, if possible at all. The method, in which a sufficiently dense target is accumulated in a trap, is tested by exposing coronene to several low charge state ion beams. Coronene belongs to the Polycyclic Aromatic Hydrocarbons (PAHs), a group of planar molecules that consist of multiple fused aromatic rings. PAHs are believed to be widely present in the Interstellar Medium (ISM) and therefore their stability, dynamics and interaction properties are of great interest in astrophysics. The coronene molecules are created by electrospray ionization and trapped in a Paul trap, where the coronene is exposed to an ion beam. The amount of coronene loss is related to the exposure to the ion beam; the cross section is determined by varying the irradiation time. The cross section could be determined for several ions with kinetic energies in the range of 2 to 25 keV/amu. There is no energy-dependence up to 20 keV/amu, but there is a charge state-dependence, which is in agreement with the theory. The cross sections for ion charge states 1+ and 2+ are $6.5 \pm 0.4 \cdot 10^{-15} \text{ cm}^2$ and $10.9 \pm 0.5 \cdot 10^{-15} \text{ cm}^2$ respectively.

Contents

1	Introduction & Theory	4
1.1	PAHs	4
1.2	Measurement of the cross section	4
1.3	Classical over the barrier model [10, 11]	5
1.3.1	Model Forsberg et al.	7
2	Experimental setup [14, 15]	9
2.1	Electrospray ionization [17, 18]	9
2.2	Funnel	11
2.3	Principles of RF filtering and trapping [22]	11
2.4	Time-of-flight mass spectrometry and detection	14
2.5	ECRIS and the ion beam	17
2.5.1	Influence of the Paul trap on the ion beam: a simulation	17
3	Results and discussion	22
3.1	Total cross sections	22
3.2	Mass spectra	27
4	Conclusion	30
5	Acknowledgements	31
A	Settings	34
B	Cross section fits & Mass spectra	35

1 Introduction & Theory

1.1 PAHs

Polycyclic Aromatic Hydrocarbons (PAHs) form a group of molecules solely composed of multiple fused aromatic rings. PAHs are planar molecules and are neither very reactive nor very soluble. They are produced in incomplete combustion processes and can be found on burnt meat and as a main component of soot (as PAH clusters), which is a pollutant of the environment. Many PAHs are also carcinogenic, forming a substantial cancer risk for workers in industries like metal foundries and tar distillation [1]. Because of these risks for the human health and the environment, PAHs are closely monitored [2]. Also, PAHs are believed to be abundant in space, because infrared (IR) emission spectra of galactic sources and the interstellar medium (ISM) contain features also seen in IR emission spectra of (large) PAHs [3]. The ISM is exposed to UV photons and beams of light ions (He^+ , H^+) of energies in the range of 10 eV to 10 keV from stellar winds and supernovae explosions [3, 4]. For that reason, several experiments on the interaction of PAHs with UV photons [5] and keV ions [6] have been done.

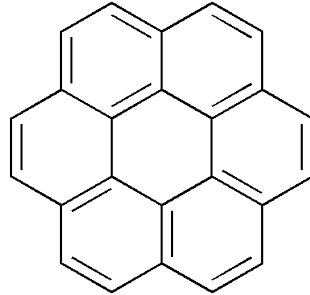


Figure 1: Schematic representation of a coronene molecule

In this thesis, absolute cross sections of interactions of ions with molecules, leading to loss (by e.g. ionization or destruction) of the molecules, for several ion beams with kinetic energies in the range of 2 to 25 keV/amu on one specific PAH cation, coronene ($\text{C}_{24}\text{H}_{12}$), are determined by a method based on recent work at the ZernikeLEIF facility by von Zastrow et al. [7]. The results are compared with the predictions of theoretical models. The accuracy and reliability of the method is also tested. The great asset of this method is that it can be used for molecules for which it is hard to produce a dense target. Coronene, a compact PAH in the form of a hexagon of aromatic rings (figure 1), is used because it is a relatively easy PAH to electrospray (see section 2.1); the molecule has been the subject of several experiments [8, 9]. In the remainder of this section, the method for the measurement of the cross section and the model for the cross section is explained. In section 2, the experimental setup is described; the results for the cross section measurements and mass spectra are presented and discussed in section 3.

1.2 Measurement of the cross section

The target molecules are accumulated in a trap (see section 2.3) until the target is dense enough for a proper S/N-ratio and then irradiated by an ion beam (see figure 2). The target molecules are ionized and fragmented due to the ion beam. The cross section can be determined by relating the amount of target loss to the area number density of ions (fluence) of the crossing ion beam. The number of molecular target ions N in the trap is related to the fluence Φ as

$$N(\Phi) = N(0)e^{-\sigma\Phi} \quad (1)$$

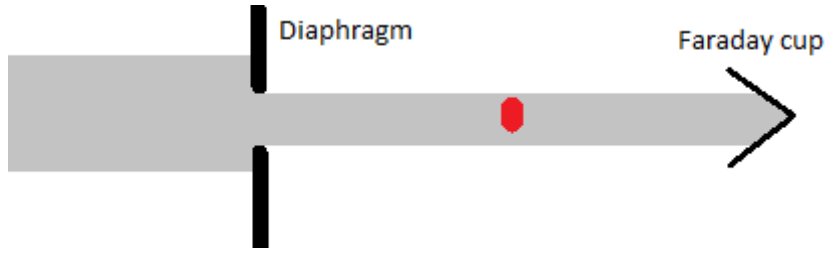


Figure 2: The ion beam (gray) irradiates the molecular target cloud (red) in the center of the trap. The current density is determined by the beam current measured in the Faraday cup and the diameter of the diaphragm. The area of the ion beam is limited to the size of the diaphragm. For a proper determination of the cross section, it is important that the ion beam completely overlaps the aperture of the diaphragm and the target cloud.

in which σ is the cross section of all processes leading to loss of the target ions. The fluence Φ has dimensions of number of particles/area and is given by:

$$\Phi = \frac{jt}{q} \quad (2)$$

In this equation, q is the charge of the ions in the projectile beam, t is the irradiation time and j is the current density (the current per unit area). The current density is determined by dividing the beam current measured in the Faraday cup (placed after the Paul trap) by the area of the ion beam. The area of the ion beam is limited to the size of the diaphragm in front of the Paul trap; this diaphragm is circular and has a radius of 0.5 mm. It is important for the determination of the cross section that the size of the ion beam does not change in the Paul trap, otherwise the current density can not be determined properly (see section 2.5.1). It is also important that the beam is homogeneous. The cross section can be determined by measuring the ratio $\frac{N(\Phi)}{N(0)}$ and fitting the equation

$$\ln \frac{N(\Phi)}{N(0)} = -\sigma\Phi \quad (3)$$

The fluence is varied by varying the irradiation time. The size and density of the ion cloud do not influence the determination of the cross section, as long as the target cloud is completely covered by the ion beam.

1.3 Classical over the barrier model [10, 11]

The cross sections are determined for projectile ions with kinetic energies in the range of 2 to 25 keV/amu. In this range, interactions are dominated by electron capture by the projectile ion as long as the orbital velocity of the least bound electron of the coronene exceeds the velocity of the ion by far. When the ion velocity is larger than the classical orbital velocity of the electron, ionization is the dominant process. For a coronene cation with an ionization potential (IP) of 10.77 eV, the classical orbital velocity of the target electron corresponds to ~ 20 keV/amu. This energy is only reached in this thesis for higher energy proton beams.

The electron capture is often explained by the classical over-the-barrier model (OVB). This is a model for the electron capture of an atomic target, but can be used as an approximation for a molecular target (see section 1.3.1 for a modified OVB-model for molecules like coronene). In the OVB-model, a charged ion approaches the target, lowering the potential barrier between the target

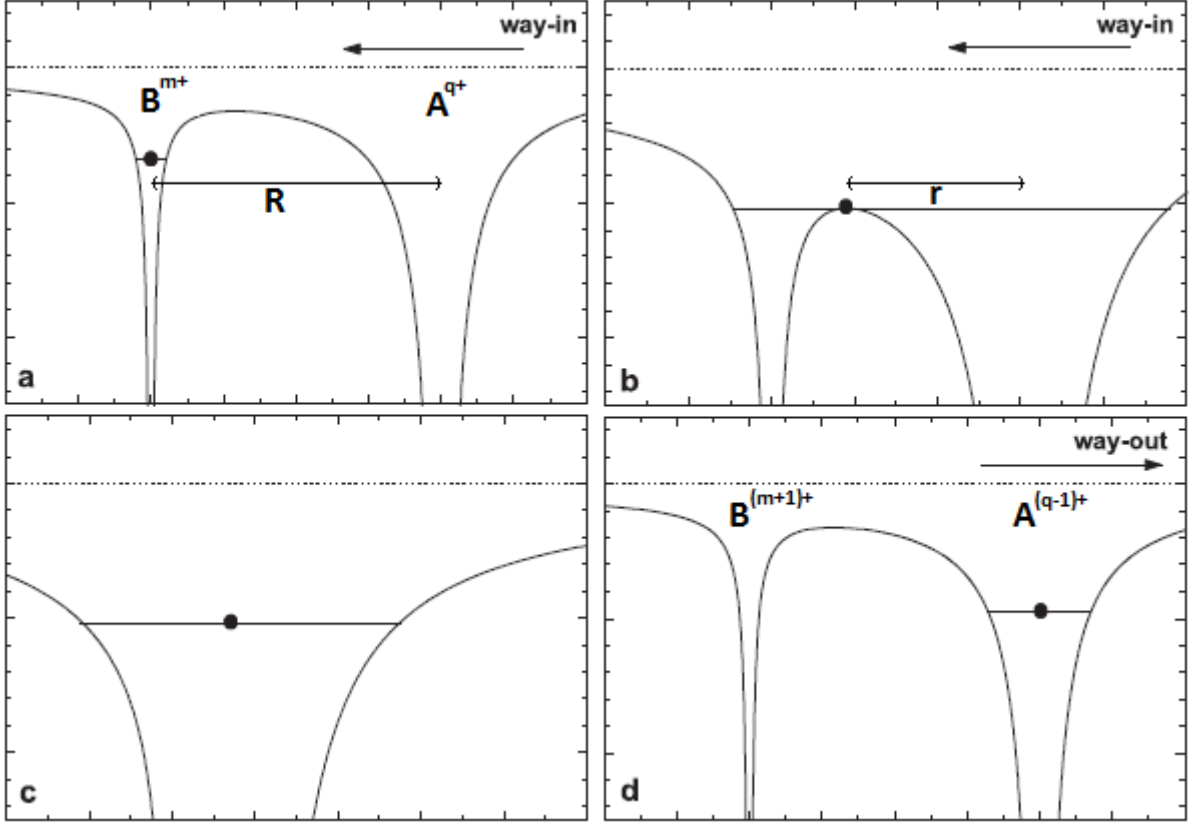


Figure 3: The OVB-model in three steps (for an atomic target): (a) The ion A^{q+} approaches the molecular target ion B^{m+} , which lowers the potential barrier. (b&c) When the potential barrier is low enough (i.e. lower than the IP), the electron transits the barrier from the target to the ion. (d) The ion moves away, the potential barrier gets higher and the electron is captured by the ion. Figure adapted from [10].

and the ion. When the potential barrier is low enough, an electron of the target can transfer to the ion and the ion captures the electron. Single electron capture from a m -fold charged target is described as follows:



When the ion (A^{q+}) approaches the target (B^{m+}), the potential seen by the active electron is described as follows:

$$V(r) = -\frac{q}{r} - \frac{m+1}{R-r} \quad (5)$$

where r is distance between the ion and the electron and R the distance between the ion and the target. The maximum of the potential is found by solving $dV/dr = 0$:

$$r_{max} = \frac{R}{1 + \sqrt{\frac{m+1}{q}}} \quad \& \quad V_{max} = -\frac{(\sqrt{q} + \sqrt{m+1})^2}{R} \quad (6)$$

If $V_{max} < E_{binding}^{el}$, the electron can transit the barrier and be captured by the ion. The binding

energy of the electron is Stark-shifted by the Coulomb field of the incoming ion and is therefore not equal to the ionization potential:

$$-\frac{(\sqrt{q} + \sqrt{m+1})^2}{R_c} = -IP - \frac{q}{R_c} \quad (7)$$

in which $\frac{q}{R_c}$ is the Stark shift term. R_c is the capture radius, the distance where the ion and the target are close enough for electron capture:

$$R_c = \frac{(\sqrt{q} + \sqrt{m+1})^2 - q}{IP} = \frac{m+1 + 2\sqrt{q(m+1)}}{IP} \quad (8)$$

The electron capture cross section is the area of the circle described by this capture radius:

$$\sigma_{ovb} = \pi R_c^2 = \pi \left(\frac{m+1 + 2\sqrt{q(m+1)}}{IP} \right)^2 \quad (9)$$

The experiments are done on a coronene cation ($m=1$); the cross section for $m=1$ is

$$\sigma_{ovb,m=1} = \frac{4\pi}{IP^2} (1 + 2(q + \sqrt{2q})) \quad (10)$$

This is the electron capture cross section for the capture of the first electron and also the total electron capture cross section. When multiple electrons are captured, the ionization potential is different for every electron, but the q is the same as the initial q : the already captured electron does not shield off the potential for the next electron. The cross section for the capture of the n 'th electron is the area of the capture radius for the n 'th electron minus the area of the capture radius for electron $n+1$ (on the condition of a point-like target):

$$\sigma_n = \pi(R_{c,n}^2 - R_{c,n+1}^2) \quad (11)$$

1.3.1 Model Forsberg et al.

The OVB model is useful for a rough estimate of the cross section, but is too simple in certain aspects. One of the main oversimplifications is that it assumes that the ion and the target are point-like objects. For molecules, this leads to an underestimation of the cross section, because the geometric cross section of the target is not taken into account. A coronene cation, for example, is a disc-like molecule with a diameter of 1.053 nm, while the capture radius for $q = 1, m = 1$ is only 0.65 nm. For a more accurate estimation of the electron capture cross section, Forsberg et al. [12] constructed a model in which a modification of the classical OVB model is made for planar, nearly circular molecules (like PAHs and in particular coronene). In this model, the molecules are treated as infinitely thin conducting neutral discs and the ions as point particles of certain charge. An analytical expression for the potential is determined and from this expression the saddle point in the energy potential is obtained. These saddle points are compared to the Stark-shifted ionization potential to obtain the capture distance, where the electron can be transferred from the PAH to the ion, like in the classical OVB model. More details about the derivation of the expression for the potential and the determination of the saddle points can be found in the paper of Forsberg et al. [12]. The capture distance alone is not sufficient for obtaining the cross section, because the different orientations of the molecules should also be considered. Therefore, a Monte Carlo simulation with randomly generated ion trajectories is necessary, where at each step a comparison between the Stark-shifted ionization potential and the saddle point of the potential is performed. The authors already did simulations for neutral coronene, but to compare the model to the experimental results in this thesis, simulations for charged coronene are done with the C++-program of the authors [13]. In the simulations the ionization energies are all

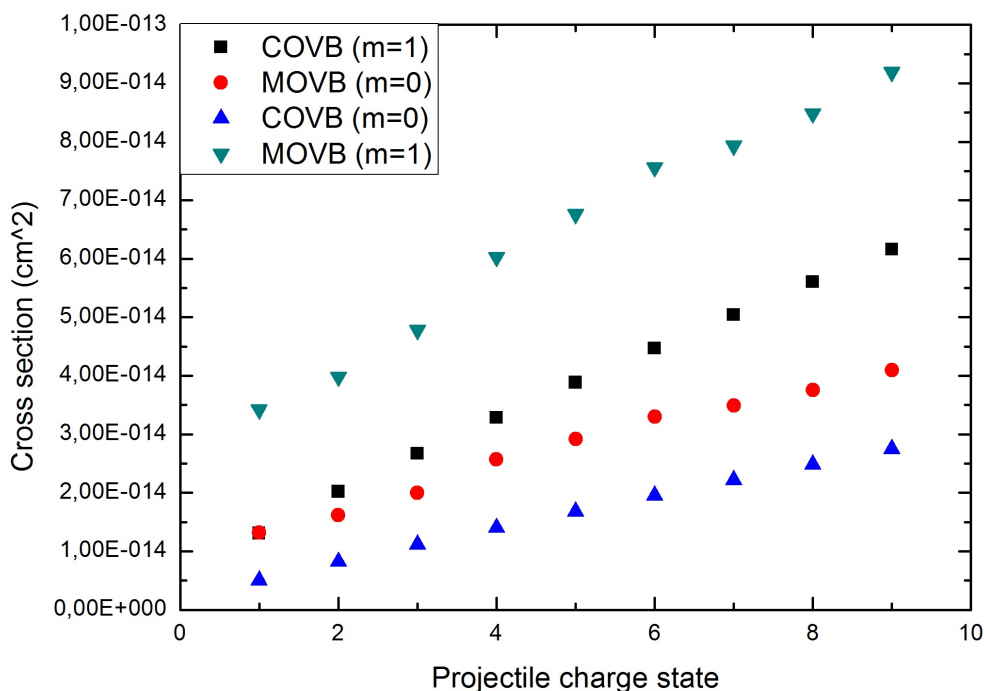


Figure 4: The cross section predictions of the classical OVB-model and the modified OVB-model for a neutral ($m=0$) and charged ($m=1$) target.

changed: the second for the neutral coronene is the first ionization energy for the coronene cation etc.. In figure 4, the results for the simulations and the prediction of the classical OVB-model are shown for charge states $1+$ to $9+$. The cross section predictions of the simulation are larger than the predictions of the OVB-model, as was expected because the simulations take the geometry into account. The ratio of the cross sections ($\frac{\sigma_{MOVB}}{\sigma_{COVB}}$) changes gradually from 2.6 for $q=1+$ to 1.5 for $q=9+$. The ratio is smaller for higher charge states because the size of the target is an important factor in the cross sections for low charge states; for higher charge states, the capture radius is larger, the target becomes more point-like and the classical OVB-model is more accurate.

The modified OVB-model assumes that the PAH is neutral. The simulations contain the change of IP, but not the change of the potential barrier due to higher charge of the target. In the classical OVB-model, the ratio of the cross sections $\frac{\sigma(m=1)}{\sigma(m=0)}$ changes gradually from 2.6 for $q=1+$ to 2.2 for $q=9+$, if the same IP is used. It is assumed that this ratio also holds for the modified OVB-model in the comparison of the experimental data to the models (see section 3). The predictions for $m=0$ and $m=1$ are for both models shown in figure 4.

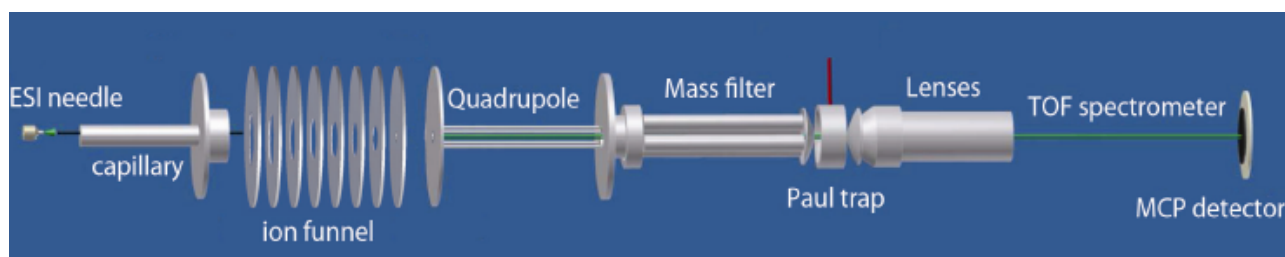


Figure 5: Schematic representation of the setup. The coronene beam (green) is guided to the Paul trap, where it is exposed to the ion beam (red). Figure adapted from ref. [16].

2 Experimental setup [14, 15]

A schematic representation of the experimental setup can be found in figure 5. The coronene is electrosprayed and focused by an RF-funnel and ejected through a diaphragm into a RF-quadrupole ion guide. After the guide, they are filtered by a mass filter and trapped and accumulated in a Paul trap. In the Paul trap, they are exposed to a beam of ions. The coronene molecules and the fragmentation products are extracted into a TOF mass spectrometer and detected by a MCP detector. The measurements are divided into cycles of two mass spectra: one mass spectrum with the electrospray on and the beam off and one with both on. One measurement series contained a couple of hundred of such cycles to obtain a spectrum in which statistical fluctuations are averaged out. In the following sections I will describe the individual parts of this setup in more detail and the influence of the trap on the ion beam is discussed.

2.1 Electrospray ionization [17, 18]

Electrospray ionization (ESI) is a good technique to bring large molecules into gas phase because there is little fragmentation, in contrary to other techniques where large molecules easily break apart. For ESI, a solution of ionized molecules is necessary. This is done in this experiment by adding 50 ml of 10 mM AgNO_3 in methanol to 1 ml saturated solution of coronene in methanol. A redox reaction with the silver ionizes the coronene. The solution is pumped at a rate of $0.16 \frac{\text{ml}}{\text{h}}$ through a capillary needle with a high potential (voltages of ~ 4 kV). A conductive liquid exposed to a high electric field gives rise to the formation of a cone (a Taylor cone [19]) of liquid at the tip of the needle. Above a certain voltage, the liquid is emitted in a jet at the top of the cone and a plume of little droplets of solvent and ions are formed. The droplets are attracted towards a capillary which is on a voltage of 100 V. During the flight at atmospheric pressure, some of the solvent evaporates and the charge density on a droplet increases (see figure 6). Eventually, the Coulomb repulsion overcomes the surface tension and the droplet breaks up in smaller droplets; the critical radius where this happens is called the Rayleigh limit. Two models (schematically depicted in figure 6) exist to explain what happens in the final phase: the charge residue model (CRM) and the ion evaporation model (IEM). In CRM, the process of evaporation and splitting repeats until all solvent is evaporated and only single ions remain. In IEM, the single ions are emitted out of the droplets individually by the strength of the electric field. There is no consensus on which model holds, although it seems that IEM is more appropriate for small organic and inorganic ions (including coronene) and CRM for larger ions like proteins [20].

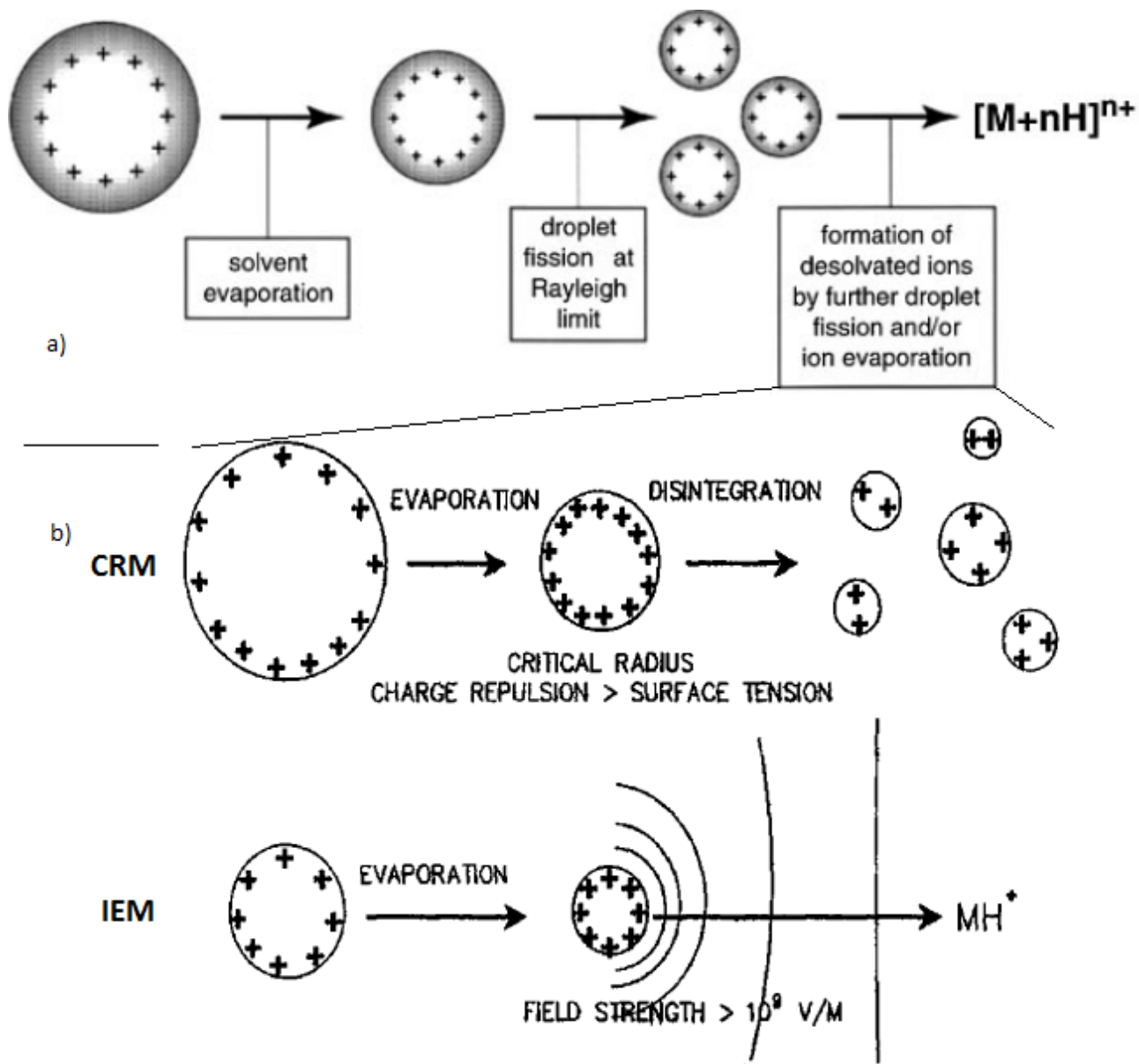


Figure 6: The principles of electrospray ionization: a) the solvent evaporates, which eventually leads the Coulomb repulsion to overcome the surface tension and breaking the droplet apart (figure adapted from ref. [17]). b) Two models explain the final phase of electrospray ionization: the Charge Residue Model (CRM) and the Ion Evaporation Model (IEM) (figure adapted from ref. [18]).

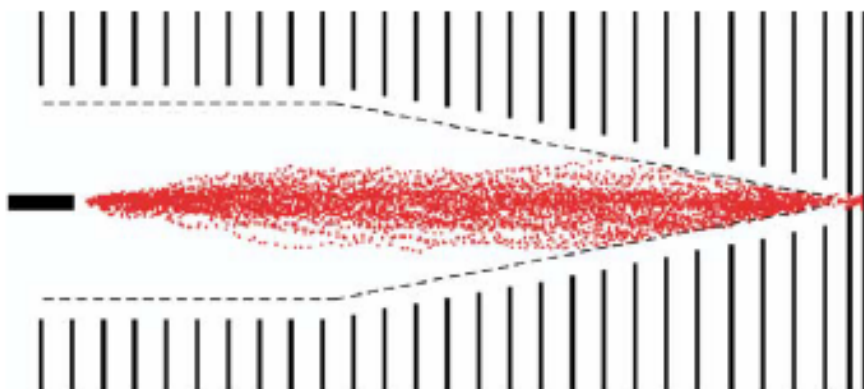


Figure 7: Simulations for the ion trajectories (red lines) in the funnel. The last two lines represent the diaphragm, the first 26 the funnel electrodes. The dashed lines are the borders of the field-free region (see figure 8). Figure adapted from ref. [21].

2.2 Funnel

The molecules enter through the capillary into the funnel chamber, where they are transported by an ion funnel. The funnel focuses the ion cloud, so that the ions can be transmitted through a small aperture (the diaphragm). The funnel design is based on the initial design of Julian et al.[21]. The ion funnel consists of 26 ring electrodes, where the inner diameter is decreasing. A radiofrequency (RF) voltage is applied on the plates, with a phase difference of 180° for two adjacent electrodes. This RF-voltage confines the ion cloud radially. The RF-field has two regions: a strong field region and an effectively field-free region. The border of these two regions is the line where the contribution of one lens to the field is cancelled out by its adjacent lenses. The distance a from the lens to this line is dependent on the spacing c between the lenses: $a = \frac{c}{\sqrt{3}}$ (see figure 8); an increase in spacing confines the cloud more. On top of the RF-voltage, a constant voltage is also applied such that a potential difference between the entrance and the exit of the funnel exists which guides the ions through the funnel. The pressure in the funnel chamber is quite high, but this is an advantage: the ions are subject to collisions due to the high pressure in the chamber, so they cool and lose kinetic energy. This compresses the ion cloud and is an advantage for further guiding and trapping. The molecules go through a diaphragm with a diameter of 5 mm to the ion guide chamber. A static voltage is applied to the diaphragm.

2.3 Principles of RF filtering and trapping [22]

The sample consists of the desired coronene cations, but also of remaining solvent, silver ions and other contamination due to the flight in the air and the funnel chamber. In order to do measurements on the molecules, the sample has to be purified and trapped. This is done in three different steps: The molecules are first transported by a 2D RF-quadrupole mass guide (also called ion guide or first quadrupole). This is done because the pressure in this chamber is too high for mass filtering and has an additional advantage that collisions focus the molecules towards the center of the ion guide and therefore it increases the transmission. This collisional focusing is explained in detail by Douglas & French [23]. After the ion guide, the molecules are guided by two electrostatic lenses (P1 and P2) into the mass filter chamber, where a 2D RF-quadrupole mass filter filters the desired sample molecules. After the filter the molecules go through an Einzel lens into a 3D RF-trap (a Paul trap), where they are trapped to be exposed to an ion beam. The molecules enter and exit the trap through 3 mm

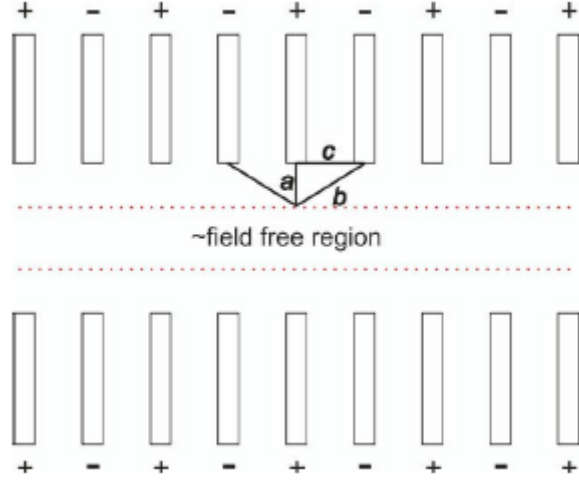


Figure 8: The funnel consists of 26 ring electrodes on which a RF-voltage is applied. There is a phase difference of 180° between two adjacent electrodes, resulting in a field-free region within the funnel. The border of the field free region is the line where the field of the center electrode is cancelled out by its neighbours. Figure adapted from ref. [21].

diameter holes in the end caps.

The principles of ion guiding, filtering and trapping are the same. The potential of an electric quadrupole field is:

$$\Phi = \frac{\Phi_0}{2r_0^2}(\alpha x^2 + \beta y^2 + \gamma z^2) \quad (12)$$

The Laplace condition requires that $\alpha + \beta + \gamma = 0$. This condition is satisfied in two dimensions with $\alpha = -\gamma = 1; \beta = 0$:

$$\Phi = \frac{\Phi_0}{2r_0^2}(x^2 - z^2) \quad (13)$$

In three dimensions this condition is satisfied with $\alpha = \beta = 1; \gamma = -2$:

$$\Phi = \frac{\Phi_0(r^2 - 2z^2)}{r_0^2 + 2z_0^2} \quad \& \quad 2z_0^2 = r_0^2 \quad (14)$$

The potential in equation 13 is generated by four linear electrodes (ideally hyperbolic shaped) which are placed on a distance r_0 to the center of the configuration. A voltage is applied between the electrode pairs (the opposite electrodes form a pair); see figure 9 for the equipotential lines and the electrode structure of the mass filter.

The potential in equation 14 is generated by a hyperbolic ring electrode in the x-y plane with radius r_0 and two hyperbolic end caps in the z-direction; the distance between the center and the end caps is z_0 . For an ideal quadrupole field, the relation between z_0 and r_0 is $2z_0^2 = r_0^2$. This is satisfied in our trap by $r_0 = 10$ mm and $z_0 = 7.07$ mm. The applied voltage on the electrodes is a dc-voltage U and a RF-voltage V with driving frequency Ω , so the potential is $\Phi_0 = U + V \cos(\Omega t)$.

In two dimensions, the equations of motion are:

$$\frac{d^2x}{dt^2} + \frac{e}{mr_0^2}(U + V \cos(\Omega t))x = 0 \quad (15)$$

$$\frac{d^2z}{dt^2} - \frac{e}{mr_0^2}(U + V \cos(\Omega t))z = 0 \quad (16)$$

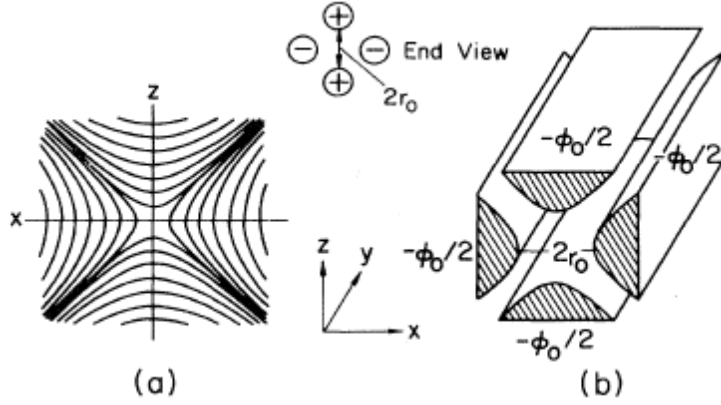


Figure 9: a) Equipotential lines for a plane quadrupole field. b) The electrode structure for the mass filter (and the ion guide). Figure adapted from ref. [22].

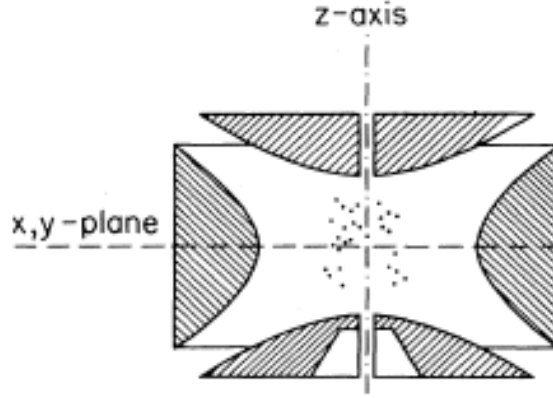


Figure 10: The structure of the Paul trap. The hyperbolic end caps are parallel to the x,y-plane, the ring electrode circumvents the z-axis. Figure adapted from ref. [22].

where e and m are respectively the charge and mass of the particle. In a homogeneous periodic electric field, the time-dependent factor cancels out, but in this quadrupole field, the average force drives the particle back to the center. These differential equations are forms of the Mathieu equation and are written in dimensionless parameters as:

$$\frac{d^2x}{d\tau^2} + (a_x + 2q_x \cos(2\tau))x = 0 \quad (17)$$

$$\frac{d^2z}{d\tau^2} + (a_z + 2q_z \cos(2\tau))z = 0 \quad (18)$$

The parameters are:

$$a_x = -a_z = \frac{4eU}{mr_0^2\Omega^2}; \quad q_x = -q_z = \frac{2eV}{mr_0^2\Omega^2}; \quad \tau = \frac{\Omega t}{2} \quad (19)$$

In three dimensions, something similar holds: $a_x = a_y = -2a_z$ and $q_x = q_y = -2q_z$. The solutions of the Mathieu equation have stability regions (see figure 11). Within these regions, the particles are

trapped in the quadrupole, while outside these regions the amplitude grows exponentially in one or more directions and the particle is lost. The parameters a and q need to be in one of the stability regions. Almost all traps and filters work in the stability region closest to the origin. The operation line $a/q = 2U/V = \text{constant}$ does not depend on the mass-over-charge ratio m/e , so all m/e lie on this line. The mass range $\Delta m/e$ can be adjusted with the dc-voltage U ; the mass range becomes smaller with an increasing U . If a/q remains constant, but U and V are changed, other m/e ratios come into the stability region, so other m/e can be selected by changing U and V proportionally.

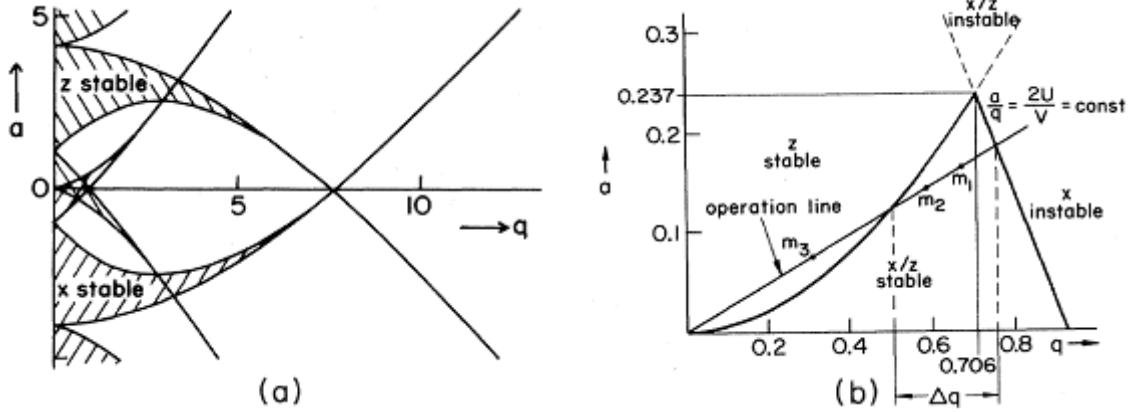


Figure 11: a) The stability figure for the 2D quadrupole field. Only ion masses for which both x and z are stable (i.e. where the regions overlap) are transmitted by the filter. b) The lowest stability region. All masses lie on the operation line; only the masses within the 'triangle' are transmitted. Δq is the mass range of the filter and can be adjusted with the dc voltage U . Figure adapted from ref. [22].

Our mass guide and Paul trap operate in RF-only mode ($U = 0$), so $a = 0$ and the operation line is the q -axis. In RF-only mode, only a particle with a m/e corresponding to a q above the q_{max} is not transmitted, so the guide and trap work as high-pass filters. Therefore, only ions above the mass cut-off (in our experiments $m/e \approx 60$) of the trap are recorded by the mass spectrometer. The end caps of the trap are grounded and a RF-voltage is applied on the ring electrode. To increase the trapping efficiency, the motions of the ions are damped after the entrance in the trap with a helium buffer gas.

2.4 Time-of-flight mass spectrometry and detection

The ions are extracted from the trap and detected in a time-of-flight (TOF) mass spectrometer. In a TOF mass spectrometer, the flight time of an ion is used for the determination of the mass-to-charge of the ion. For the extraction of the ions, the RF of the trap is switched off and a bias voltage is applied to the end caps of the trap. The ions are accelerated and focused with two extraction lenses (L1 and L2) into the TOF-tube. An ion with charge z and mass m gets the kinetic energy zU :

$$zU = \frac{mv^2}{2} = \frac{md^2}{2t^2} \quad (20)$$

where U is the extraction voltage, d the length of the TOF-tube and t the flight time of the ion. The flight time is proportional to the square root of m/z :

$$t = \frac{d}{\sqrt{2U}} \sqrt{\frac{m}{z}} \quad (21)$$

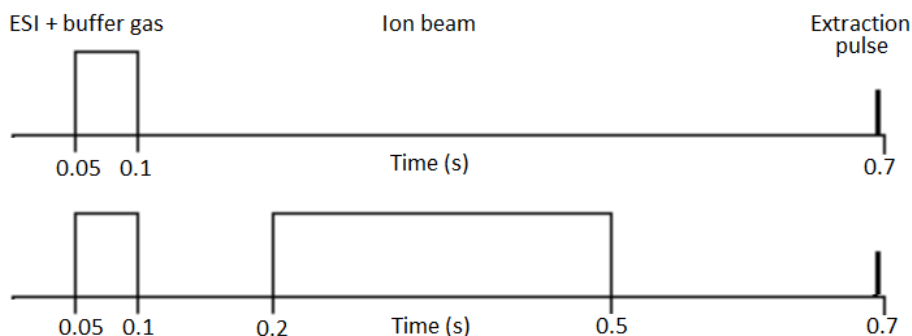


Figure 12: A typical acquisition scan, with a period of 0.7 seconds. One acquisition cycle contains two scans: in the first scan (above) the trap content is not exposed to the beam, in the second one it is. There is a delay of 50 ms between the start of the cycle and the loading of the trap with sample molecules to avoid interference with the extraction of the preceding cycle.

These equations are appropriate for the field-free region (the TOF-tube), but not for the extraction part (the lenses L1 and L2). In practice, the more general expression

$$t = k\sqrt{\frac{m}{z}} + c \quad (22)$$

is used to account for small deviations due to e.g. field imperfections. The parameters k and c are obtained by calibration to a well-known spectrum (like coronene). The geometry, length of the tube and extraction voltages are included in k , while time-offsets like the time between a hit at the anode and recording by the digitizer and the time between extraction pulse and the start of recording are included in c .

The signal is detected at the end of the tube by a microchannel plate (MCP) detector. A MCP consists of multiple channels in which the incoming ion releases multiple electrons, which in turn release multiple electrons themselves, causing an avalanche of electrons which amplify the signal. The MCP detector is stacked in a chevron formation to increase signal gain: the gain of two MCPs in chevron configuration can get as high as 10^7 , while a straight MCP can get a signal gain of 10^4 [24]. The front end of the MCP detector is biased to -5 kV, while the back end is biased to -3 kV. After the detector, a grounded anode collects the electrons and produces a signal which is recorded by a GHz digitizer for further processing and recording of the data by a Labview application. The cage of the TOF-tube is put on a constant voltage of -3 kV. In front of the detector is a grid, biased to a voltage of -3 kV.

The acquisition cycles are controlled by a pulse/delay generator (which is controlled by a Labview application) and contains two different scan cycles (see figure 12). In both cycles, the trap is loaded with molecules for 50 ms, while simultaneously the molecules are cooled by helium. The PAHs are exposed to an ion beam in one of the two cycles; the beam is blocked in the other cycle. The irradiation time is varied for our experiments in a range of 25 ms to 9.75 s. After that, the trap content is first extracted for measurement and detection by an extraction trigger pulse of 3.5 ms. This pulse also shuts off the RF-voltage of the trap at the next zero-voltage crossing; the extraction voltage has a delay of 500 μ s to allow the RF to shut off. A voltage is applied onto the end caps of the trap to guide the molecules and fragments towards the TOF-tube. A measurement contains multiple acquisition cycles where finally the average of the spectra is recorded for both of the scan cycles. The fraction of coronene loss due to the ion beam is obtained by determining the areas of the coronene peak for both scan cycles.

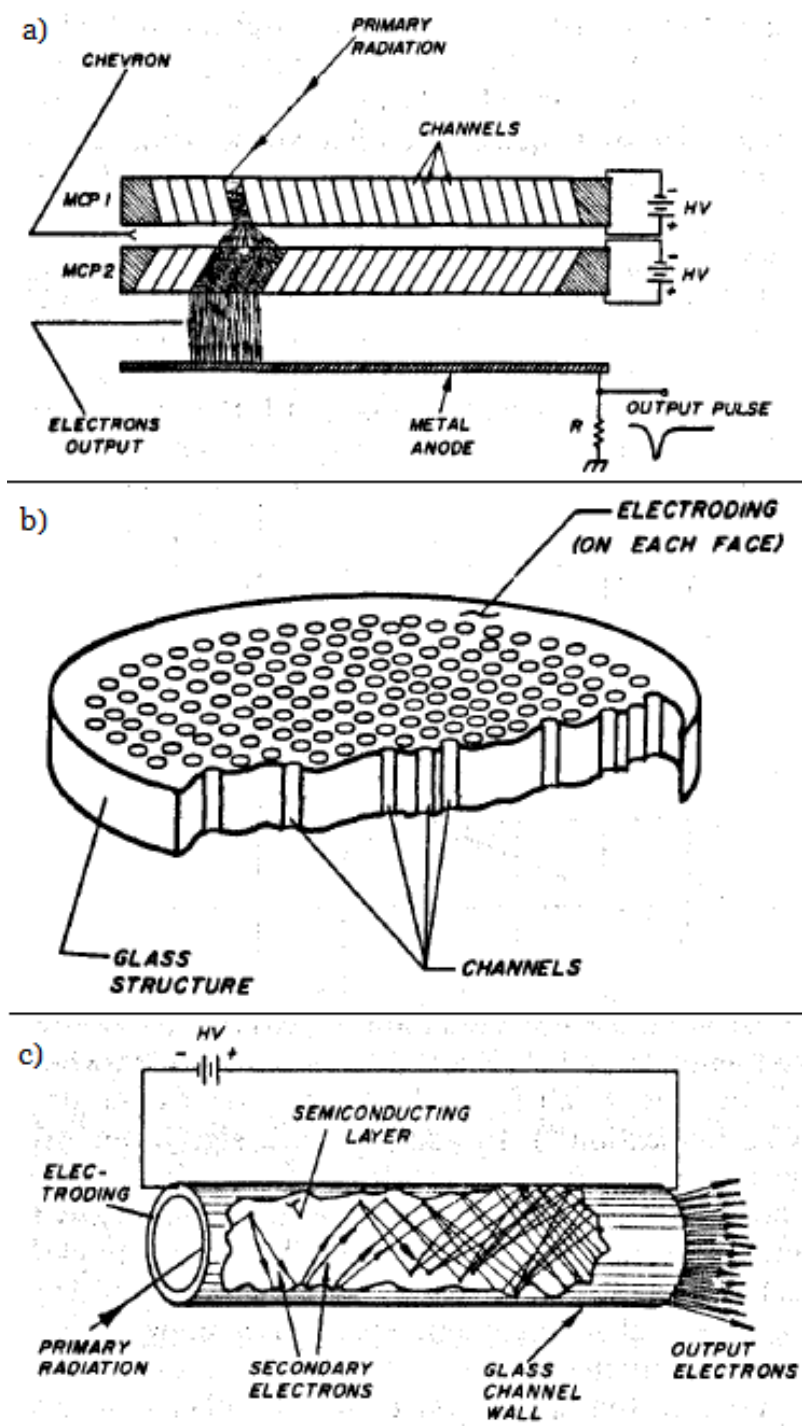


Figure 13: a) The signal of the impact of a particle (ion, neutral, electron, etc.) is amplified by two MCPs in chevron configuration; the anode collects the electron output of the channels and sends an output pulse. b) A microchannel plate contains multiple channels, in which c) incoming radiation (ions) releases multiple electrons, who in turn also release multiple electrons, causing an avalanche of electrons. Figure adapted from ref. [24].

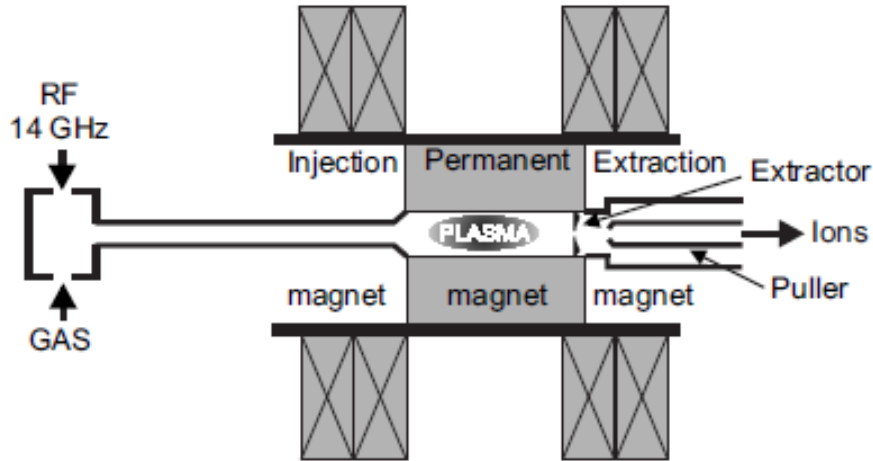


Figure 14: Schematic overview of the ECRIS

2.5 ECRIS and the ion beam

The ion beam is created in an Electron Cyclotron Resonance Ion Source (ECRIS). In the ECRIS (figure 14), a plasma is contained in a 'magnetic bottle', generated by a superposition of an axial magnetic field created by two coil magnets and a radial magnetic field created by a permanent hexapole magnet. The gas of the desired ion is injected in a vacuum chamber where a RF-field of frequency ω_{RF} is coupled. In the magnetic bottle, the plasma electrons gyrate around the field lines with the cyclotron frequency $\omega_c = \frac{eB}{m}$ where e is the fundamental charge, m the mass of the electron and B the magnetic field strength. When the cyclotron and the RF-frequency match ($\omega_c = \omega_{RF}$), the electrons are resonantly accelerated and further ionize atoms and ions. To give the ions the desired kinetic energy, the whole ion source is floated on a high voltage in range of a few kilovolts to 25 kV. A puller lens is used to extract the ions out of the source. The desired ion beam is selected by a 110° magnet. The ion beam is transported through a beamline with a series of quadrupole magnets and correction magnets and deflected to the setup with a 45° deflection magnet. The ions go through a diaphragm with a radius of 0.5 mm before entering the Paul trap. The entrance and exit of the trap are both holes in the ring electrode with a diameter of 2.4 mm. The current of the ion beam is measured with a Faraday cup installed 2 cm behind the Paul trap. A Faraday cup is a metal cone which measures the current due to the ions hitting the cup. The number of ions hitting the cup can be determined from this current and the charge of the ions. In front of the cone are two plates: one grounded plate at the front and one between the grounded plate and the cone, on which a negative voltage is applied to prevent released electrons from escaping the cup, what would lead to overestimation of the current.

2.5.1 Influence of the Paul trap on the ion beam: a simulation

The Paul trap operates on high RF-voltages (a peak-to-peak voltage (V_{p-p}) of 2000 V) and can significantly alter the shape, size and trajectory of the ion beam, especially for low-velocity ion beams. Therefore, a simulation of the ion beam in the Paul trap is done in Simion [25]. The period of the RF applied to the Paul trap is $1 \mu s$, while an individual ion travels through the Paul trap in tens of nanoseconds, so for a single ion the potential is almost constant. The simulation is done in two ways: a non-RF simulation, where the voltages are constant and the trajectories of the ions are studied for different parameter settings, and a RF-simulation, which is more crude to save computing power, but

where the RF is applied on the trap. The results for both simulations are similar.

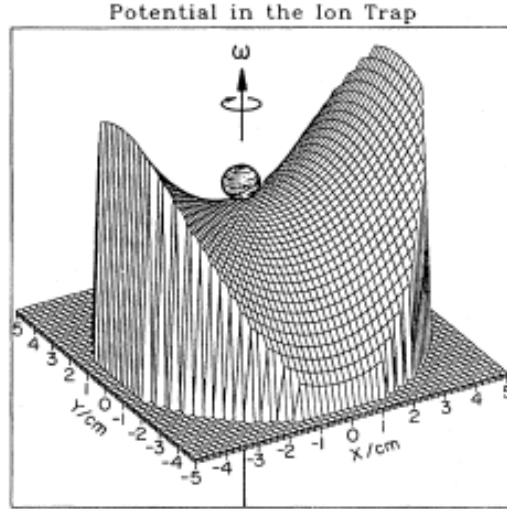


Figure 15: The trap has a saddle-shaped potential, so the ions (moving in the z -direction) will move towards the center in one direction (x -direction in this case) and away from the center in the other (y -direction in this case). Figure adapted from [22].

The potential of the Paul trap has the form of a saddle potential (figure 15), so the ions move towards the center in one direction and away from the center in the other direction: the shape of the ion beam changes from circular to ellipsoid. This can be seen in figure 17, where the position of the ions two centimeter behind the trap (the position of the Faraday cup) is shown for 15 keV He^{2+} ions with starting times during one period of RF of the trap. This is the case if the diaphragm is placed in the center with respect to the axis of the ring electrode holes. The ions will deviate relatively more when their starting position is more off-center. As long as the diaphragm is not placed off-center for more than 0.6 mm, all the ions (studied in this thesis) will go through the trap. The Faraday cup will capture all the ions as long as it is not placed off-center for more than 1.5 mm, on the condition that the diaphragm is placed in the center. Misalignment of the diaphragm or the Faraday cup can be checked by switching off the Paul trap: when there is a misalignment, the ion beam current in the cup should be higher if the trap is switched off. This is not the case for our experiment, so the diaphragm and the cup are well aligned.

Another point of interest is the shape of the ion beam. When the shape changes, the density of the beam can change or the beam can become less homogeneous. Both aspects are important in determining reaction cross sections. As seen above, the shape is significantly altered by the Paul trap, but this is mainly after the ions passed the center of the trap. At the center the beam is less deformed, because the deformation is caused mainly by the slight angle change of the direction of the ions, which is of more importance at larger distance. This can be seen in figure 16, where the position of the ions in the center of the trap for starting times within one period of RF is displayed. It should be kept in mind however that deformation of the beam can cause inaccuracy of the determination of the cross sections.

An interesting influence of the trap is the change in kinetic energy. In figure 18, the kinetic energy of an ion at four (at the minimum, the maximum and at zero with increasing and decreasing voltage) different moments of the period of the RF is depicted. The ions have the potential barrier of the Paul trap to overcome, resulting in an increase/decrease of kinetic energy. The potential difference is the strongest at the entrance and exit of the trap (the holes in the ring electrode). After the trap, the

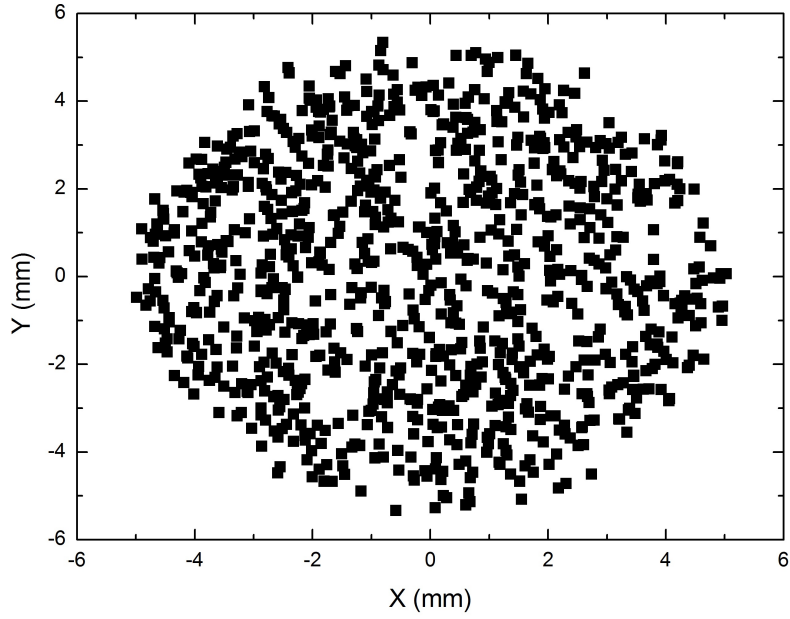


Figure 16: The simulated positions of 15 keV He²⁺ ions at the center plane of the trap. The ion beam is not yet deformed at the center of the trap. The ions starting position was within a circle of radius 5 mm around the origin.

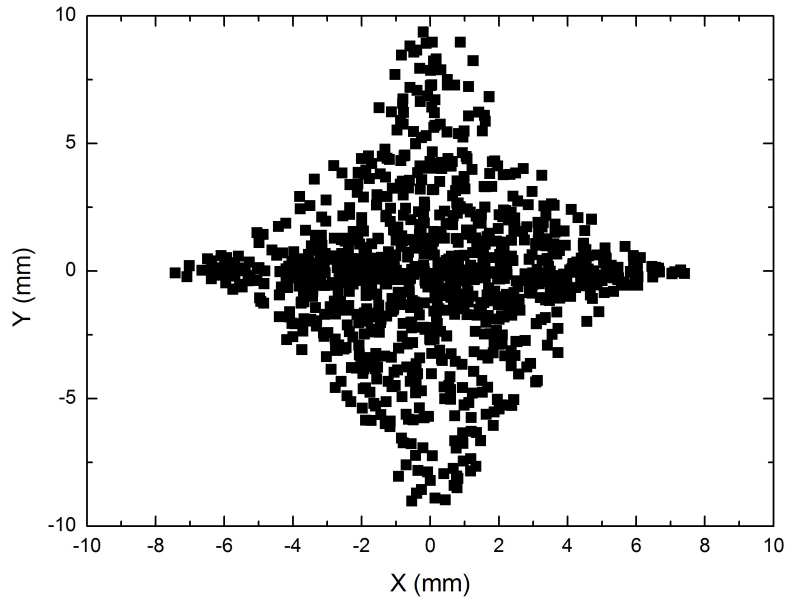


Figure 17: The simulated positions of 15 keV He²⁺ ions at 20 mm behind the trap for starting times within one period of RF of the trap ($V_{p-p}=2000V$). The cross-shape is caused by a superposition of two ellipsoids: one half of the period the ions form an ellips stretched in the x-direction; the other half they form an ellips stretched in the y-direction. The ions starting position was within a circle of radius 5 mm around the origin.

potential goes back to the initial value. The voltage on the ring electrode is slightly different for the entrance and exit of the ion beam, because entrance and exit is obviously not at the same time. This causes a difference in the kinetic energy of the ions after the trap. This effect is the largest if the derivative of the RF voltage is the highest, i.e. when the potential of the ring electrode is near ground potential.

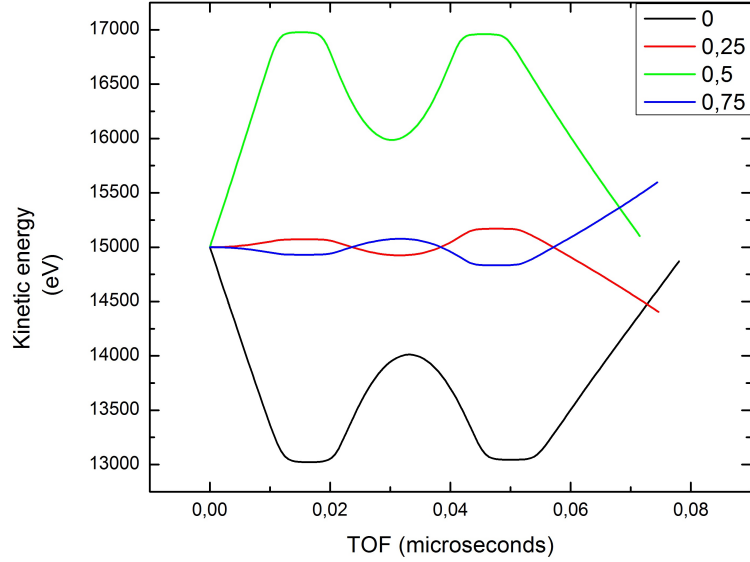


Figure 18: The final kinetic energy of four 15 keV He^{2+} ions at the position of the Faraday cup after passage through the trap. The deviation with respect to the initial kinetic energy is the highest for the two ions who transit the trap when the RF-voltage is near zero (0.25 and 0.75 of a period). At 0 of a period, the trap voltage is at his maximum; at half period, the trap is at his minimum. The peak-to-peak voltage is 2000V.

In the center of the trap, the potential is weaker, only half of the potential difference of the end caps and the ring electrode. The spread in kinetic energy in the center is $\frac{qV_{RF}}{2}$, where q is the charge of the ions of the ion beam and V_{RF} the voltage on the trap. This spread is used as the uncertainty of the energy in the results. In figure 19 is a histogram of the distribution of kinetic energies of the ions in the center of the trap. The distribution does not maximize at the mean of the kinetic energy, but at the maximum and minimum. Most of the time the voltage of the trap is in the region where the time-derivative of the voltage is around zero, which is at the maximum/minimum of the voltage because the voltage is driven by a sinusoid. This should be kept in mind in the discussion about the energy-dependence of the cross section results: a quantitative conclusion about an energy-dependent effect can only be given with the uncertainty of this spread. This should also be considered in other experiments with this setup in case energy-dependence is important.

It should be noted that in the simulations it is assumed that the beam is circular and homogeneous. Also, only simulations are conducted for ion beams of energies and ions used in the real experiment. For lower energies the beams are more deflected and deformed.

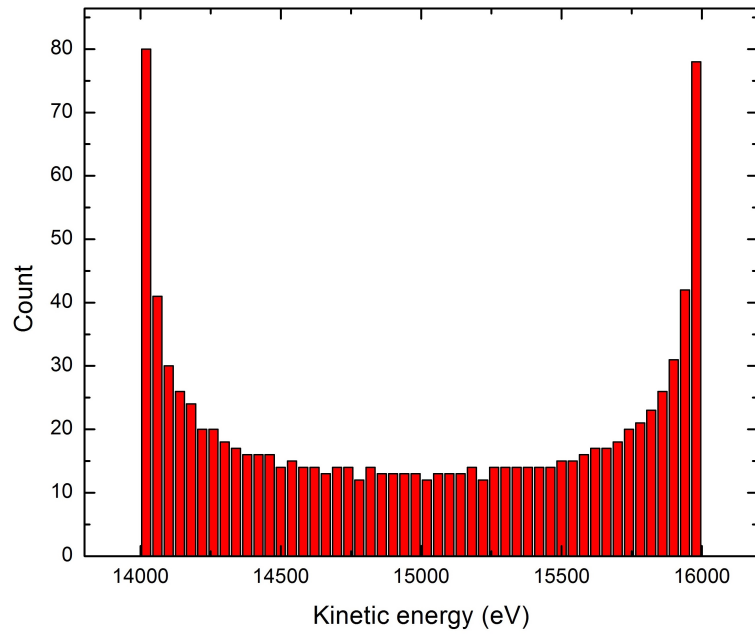


Figure 19: A histogram of the distribution of kinetic energies in the center of the trap of 1000 ions probing one period of the RF-voltage ($V_{p-p}=2000V$) of the trap. The bin width is 40 eV.

3 Results and discussion

In this section, the results are presented and discussed. The main part of the section is a discussion of the cross section results and a comparison to the models. A discussion of the fragments in the mass spectra of these measurements is at the end of this section.

3.1 Total cross sections

A mass calibration is executed for the obtained mass spectra. The area of the $m/z = 300$ peak (the coronene cation peak) is determined for all spectra; the natural logarithm of the ratio of the irradiated and the non-irradiated peak area is taken for the determination of the cross sections. These natural logarithms of the ratios are plotted against the fluence and a linear fit is done to obtain the cross sections and their fitting errors (see equation 3 in section 1.2). In figure 20, an example of one of the fits is shown. The complete collection of cross section fits is presented in appendix B. The fits are forced to go through the origin, although the results do not differ much from the non-fixed fits.

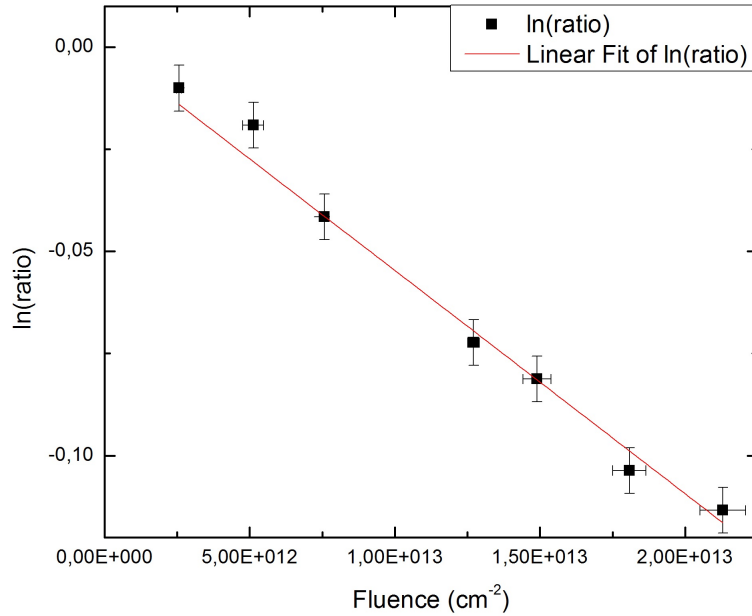


Figure 20: An example of one of the cross section fits (20 keV H^+ on coronene⁺). The natural logarithm of the ratio of irradiated and non-irradiated peak areas is fitted to the fluence (see equation 3 in section 1.2). The cross section of this particular ion is $5.5 \pm 0.1 \cdot 10^{-15} \text{ cm}^2$.

The uncertainty in the natural logarithms of the ratios is determined by a test measurement of 512 non-irradiated coronene spectra, where the standard deviation of the distribution of coronene peak areas is determined with the appropriate uncertainty propagation laws. The relative error of the fluence is estimated to be the relative error of the beam current, because that error is expected to be dominant with respect to other errors in the fluence equation (eq. 2), like the error in the diaphragm size and in irradiation time. The error in the beam current is estimated, where fluctuations of the beam current and increase/decrease of the current during the experiment are considered. Sometimes, when the irradiation time is long enough, i.e. when the shutter in the beam line is open long enough, the beam current could be monitored during the experiment and a better estimation for the error could be made. The errors are used as weighting factors in the fitting procedure (least-square method). The

uncertainty of the kinetic energy of the ion beams is the spread in energy due to the Paul trap ($\frac{qV_{RF}}{2}$, see section 2.5.1); the uncertainty (in keV/amu) is bigger for ions with a higher charge state and/or a lower mass. It should be noted that this uncertainty is not a statistical error with a 1σ -error bar, but the error bars represent the boundaries where the energy (should) lie within.

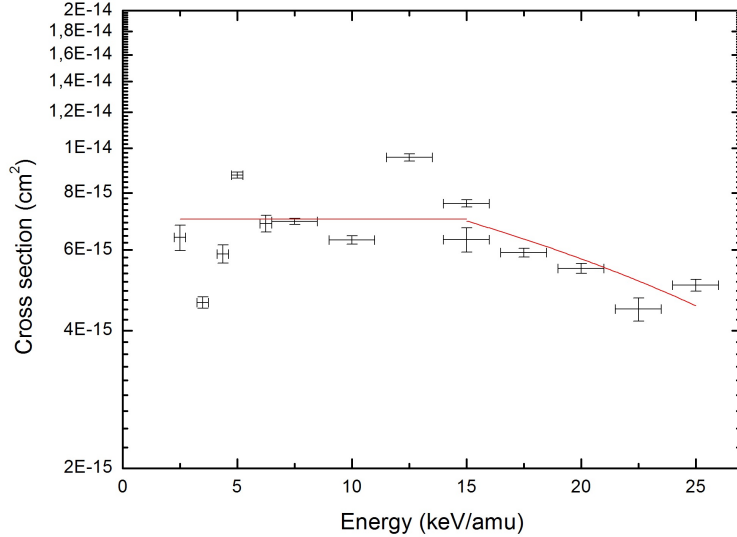


Figure 21: All the cross sections for charge state $q=1+$. The capture cross section is expected to decrease for ion velocities higher than the classical orbital velocity of the coronene electron (~ 20 keV/amu).

The cross sections, the weighted average for each ion and their fitting errors are listed in table 1 (page 25) and plotted in figure 22 (page 24). There seems to be no energy dependence for the cross sections, with a possible exception for the protons, where the cross sections seem to decrease for increasing ion energy, especially for the higher ion energies (see figure 21 for a combined plot of the He^+ and H^+ cross sections and their energy dependence). This is in agreement with the theory, which predicts no energy dependence in the electron capture energy range. The protons have kinetic energies around the energy corresponding to the classical orbital electron velocity of the coronene (20 keV/amu). Above this energy, ionization becomes more dominant; ionization processes have lower cross sections and offer an explanation for the decrease of the cross sections of the protons.

The equal cross sections for He^+ and H^+ suggests that there is also no ion-dependence for the total loss cross sections. Considering the data for charge state $1+$ and $2+$, there is a dependence on the charge of the ions, as expected. Compared to the cross sections for the different charge states predicted by the OVB-model and the model of Forsberg et al. (figure 23, page 26), the experimental cross sections are lower than both the OVB-cross sections and the cross sections of the Forsberg-model. The dependence of the He^{2+} -, He^+ - and H^+ -cross sections is similar to the cross sections of the models. The models overestimate the cross section; this can be caused by oversimplifications (e.g., the models do not take recapture of the electron by the target into account).

The cross sections of the O^{5+} and the O^{6+} ions are very small in comparison with the helium and proton cross sections, considering their higher charge state. There seems to be systematic lower determinations of these cross sections. It was very hard to get and maintain a proper oxygen ion beam through the trap during the experiments and required much focusing of the beam by the guiding and correction magnets. It could be that this caused the beam to be not completely parallel and homogeneous or that the beam did not cover the whole target cloud, resulting in lower cross section

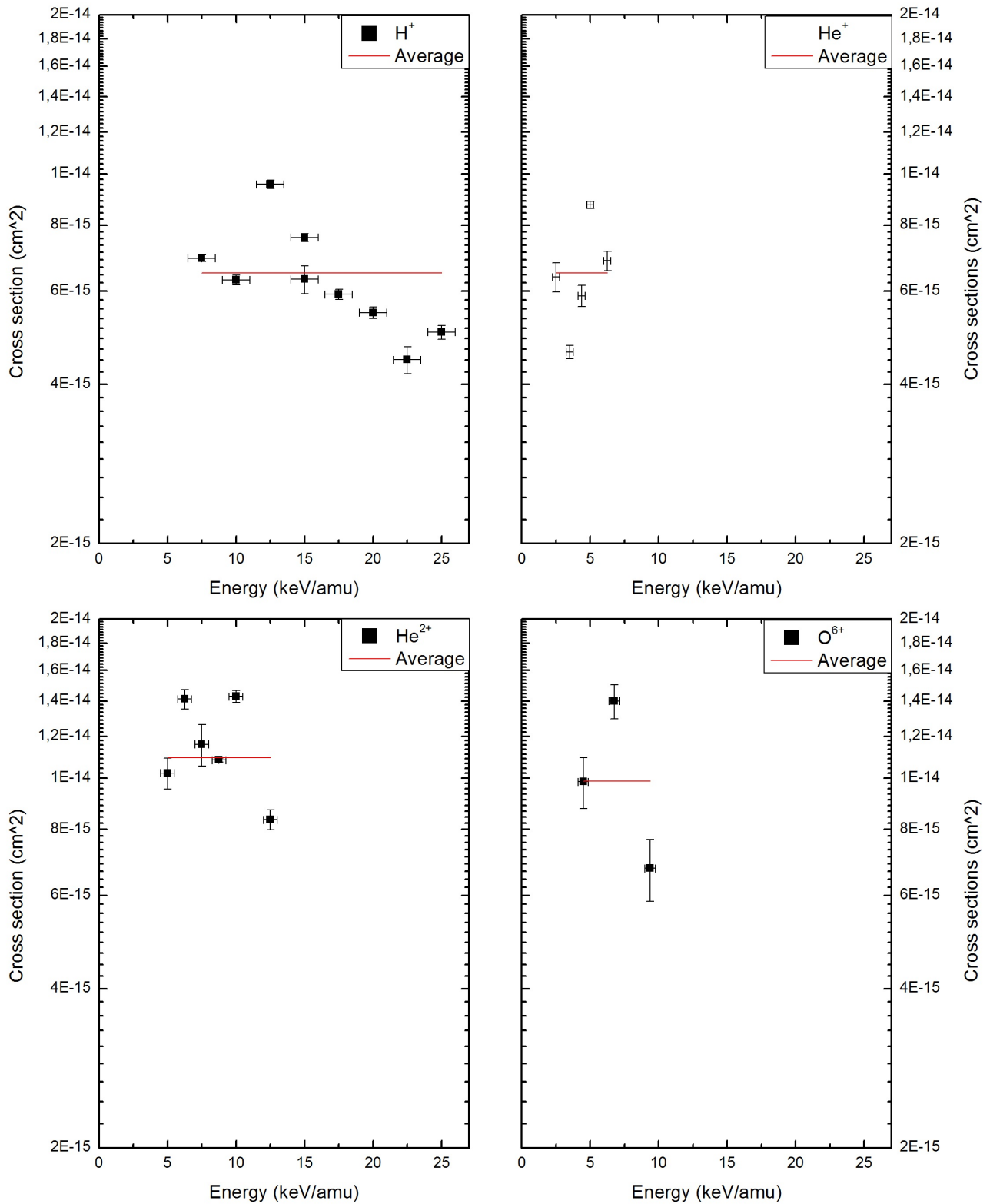


Figure 22: The cross sections and the weighted average for the different ions. O⁵⁺ is, as a single point, not included in the figure.

Energy & ion	Cross section & error (cm ²)
7.5 keV H ⁺	6.9 ± 0.1 10 ⁻¹⁵
10 keV H ⁺	6.3 ± 0.1 10 ⁻¹⁵
12.5 keV H ⁺	9.6 ± 0.2 10 ⁻¹⁵
15 keV H ⁺	6.3 ± 0.4 10 ⁻¹⁵
15 keV H ⁺	7.6 ± 0.1 10 ⁻¹⁵
17.5 keV H ⁺	5.9 ± 0.1 10 ⁻¹⁵
20 keV H ⁺	5.5 ± 0.1 10 ⁻¹⁵
22.5 keV H ⁺	4.5 ± 0.3 10 ⁻¹⁵
25 keV H ⁺	5.0 ± 0.2 10 ⁻¹⁵
Weighted average H ⁺	6.5 ± 0.4 10 ⁻¹⁵
10 keV He ⁺	6.4 ± 0.4 10 ⁻¹⁵
14 keV He ⁺	4.6 ± 0.1 10 ⁻¹⁵
17.5 keV He ⁺	5.9 ± 0.3 10 ⁻¹⁵
20 keV He ⁺	8.7 ± 0.1 10 ⁻¹⁵
25 keV He ⁺	6.9 ± 0.3 10 ⁻¹⁵
Weighted average He ⁺	6.5 ± 0.9 10 ⁻¹⁵
20 keV He ²⁺	1.02 ± 0.07 10 ⁻¹⁴
25 keV He ²⁺	1.41 ± 0.06 10 ⁻¹⁴
30 keV He ²⁺	1.2 ± 0.1 10 ⁻¹⁴
35 keV He ²⁺	1.08 ± 0.01 10 ⁻¹⁴
40 keV He ²⁺	1.43 ± 0.04 10 ⁻¹⁴
50 keV He ²⁺	8.3 ± 0.4 10 ⁻¹⁵
Weighted average He ²⁺	1.09 ± 0.05 10 ⁻¹⁴
75 keV O ⁵⁺	7.7 ± 0.2 10 ⁻¹⁵
72 keV O ⁶⁺	9.6 ± 1.1 10 ⁻¹⁵
108 keV O ⁶⁺	1.4 ± 0.1 10 ⁻¹⁴
150 keV O ⁶⁺	6.8 ± 0.9 10 ⁻¹⁵
Weighted average O ⁶⁺	9.9 ± 2.2 10 ⁻¹⁵

Table 1: The cross sections and their fitting errors for the ions H⁺, He⁺, He²⁺, O⁵⁺ and O⁶⁺

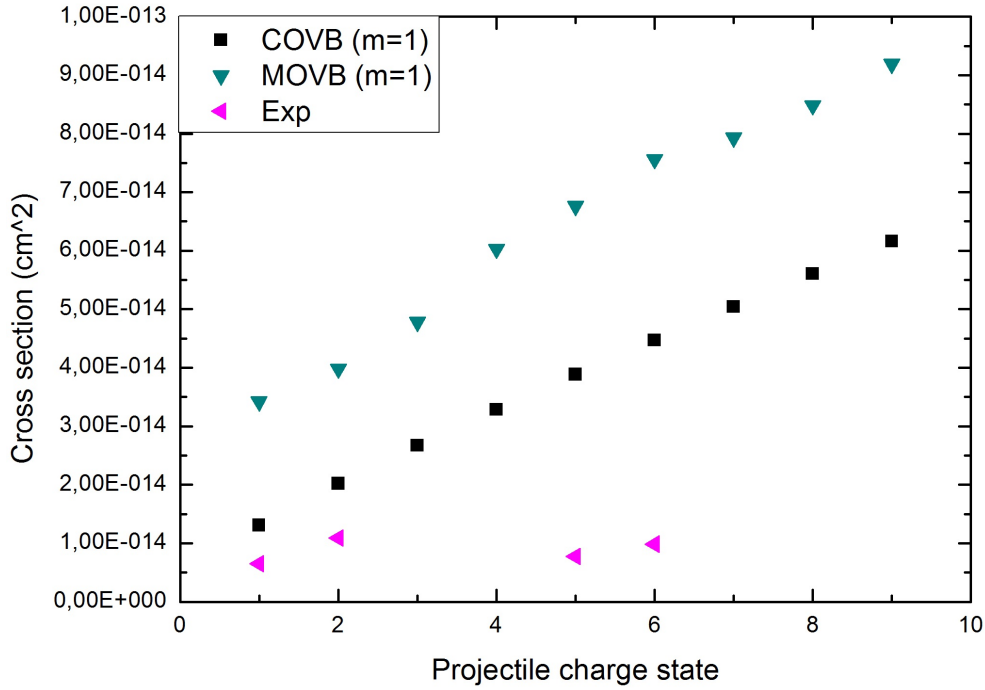


Figure 23: The cross section predictions of the classical OVB-model and the modified OVB-model and the actual experiments.

determinations.

The determination of the cross sections for the O^{5+} and the two lowest cross sections of the O^{6+} are the last experiments conducted and it could be that the background together with the fragments pushed the coronene out of the trap. Since the amount of background decreases after a long period of measurements, it offers a (partial) explanation for the higher cross sections for the earlier measured cross sections. However, there is no correlation between the size of the cross sections and the date of the experiment (except for the three cross sections described above). There is also no correlation between the size of the cross sections and the ion beam current. The date of experiment and the beam current can be found together with the fits of the cross sections in appendix B.

In earlier test measurements, also some cross sections are determined; one each for He^+ and He^{2+} and four for O^{6+} . These cross sections are not very precise and accurate due to an unstable coronene beam and due to the fact that no voltage was applied at the entrance of the Faraday cup, leading to an overestimation of the ion current and an underestimation of the cross section. Nevertheless it can be used to get an estimation of the order of magnitude for the cross sections with oxygen. The cross sections are listed in table 2. The cross section for 60 keV O^{6+} is high because the ion current is not accurately measured. The Faraday cup was placed at a larger distance of the trap and did not collect the whole ion beam, but only $\sim 85\%$ (the difference of the current with the trap turned on and off). Corrected with this value, the cross section for 60 keV O^{6+} is $3.4 \cdot 10^{-14} \text{ cm}^2$. The helium cross sections are lower, due to the overestimation of the ion current, but are in line with the other cross sections for He^+ and He^{2+} . Considering the deviation of the helium data and the average of the cross sections in these test measurements, the cross section of O^{6+} is estimated to be somewhere around $3 \cdot 10^{-14} \text{ cm}^2$, which is more in line with the predictions of the models and the cross sections found for the lower charge states.

The used method is a good method to get a rough estimate (a standard deviation of $\sim 10\%$,

Energy & ion	Cross section (cm ²)
60 keV O ⁶⁺ *	3.4 10 ⁻¹⁴
90 keV O ⁶⁺	1.2 10 ⁻¹⁴
120 keV O ⁶⁺	3.2 10 ⁻¹⁴
150 keV O ⁶⁺	2.5 10 ⁻¹⁴
20 keV He ⁺	4.7 10 ⁻¹⁵
40 keV He ²⁺	9.4 10 ⁻¹⁵

Table 2: The cross sections found in the test measurements. *: see text for a remark about this cross section.

depending on the amount of measurement time) of the cross section of these interactions, but for a more precise determination a more sophisticated method is necessary. The 1σ fitting error for the helium and proton cross sections is between five and fifteen percent of the found value. The measurements can be improved by a better ion beam, a more stable electrospray signal with less uncertainty and, if possible, a way to check the shape and size of the beam and the overlap of the ion beam with the diaphragm and the target cloud. The predictions of the models for the cross sections are higher than the experimental results, but the dependence on the charge state is similar.

3.2 Mass spectra

In the test measurements for the cross section measurements, also mass spectra for different ions and energies are recorded. These measurements were done in a three-scan cycle, with an additional background measurement which is subtracted of the fragmentation spectra. In figure 24, three of these spectra are shown; the other spectra are in appendix B. The spectra are normalised to the highest peak in the spectrum, most often the dication peak. The spectra are quite similar for different kinetic energies of the same ion. In the He⁺ spectra are clearly several peak groups visible around $m/z = 74, 86, 98, 110, 122, 134$ and 146 (the 146 -peak group overlaps with the dication peak; see later on). These peak groups are C_xH_y fragments, where each peak group belongs to a certain x number of C-atoms. These peak groups are also found by Lawicki et al. [8], who obtained mass spectra for ions-on-coronene with a different ionization technique (oven evaporation) and found mostly fragments below our mass cutoff of $m/z \sim 60$. The $m/z = 91$ peak is a background contamination peak of unknown origin. The peak around $m/z = 157$ is probably a double ionized coronene and water cluster, although it could also be $C_{13}H_y$. The $m/z = 100$ and $m/z = 150$ peaks are the trication and dication of coronene respectively. The mass spectra of He²⁺ show the same peak groups, but the dication and trication peaks are higher with respect to the other peaks. The spectra of O⁶⁺ have a bad S/N-ratio; the only peaks visible apart from noise and contamination are the dication and trication peaks.

The dication coronene peak resulting of collisions of He⁺ on coronene⁺ is showing hydrogen loss up to 8 hydrogen atoms ($m/z = 146$). The dication is losing hydrogen in even numbers (the peaks appear at integers), so the dication favors 2H- or H₂-loss above single H-loss.

When He²⁺ and O⁶⁺ projectiles are used the dication peaks do not show this amount of hydrogen loss, featuring both only a small $m/z = 149$ peak. The capture distance for the He⁺ is smaller and therefore the relative cross section for processes other than electron capture are larger. The hydrogen loss peaks decrease with respect to the $m/z = 150$ peak for increasing ion energy (see figure 25). Hydrogen loss is not clearly seen in the trication peak, because the trication peak has an overlap with the C_8H_y peak group. For the dication the nearest peak group is around $m/z = 146$, but these peaks are very small and barely influence the peak heights of the hydrogen loss peaks. Hydrogen loss of the dication is also observed in interactions with photon beams [26].

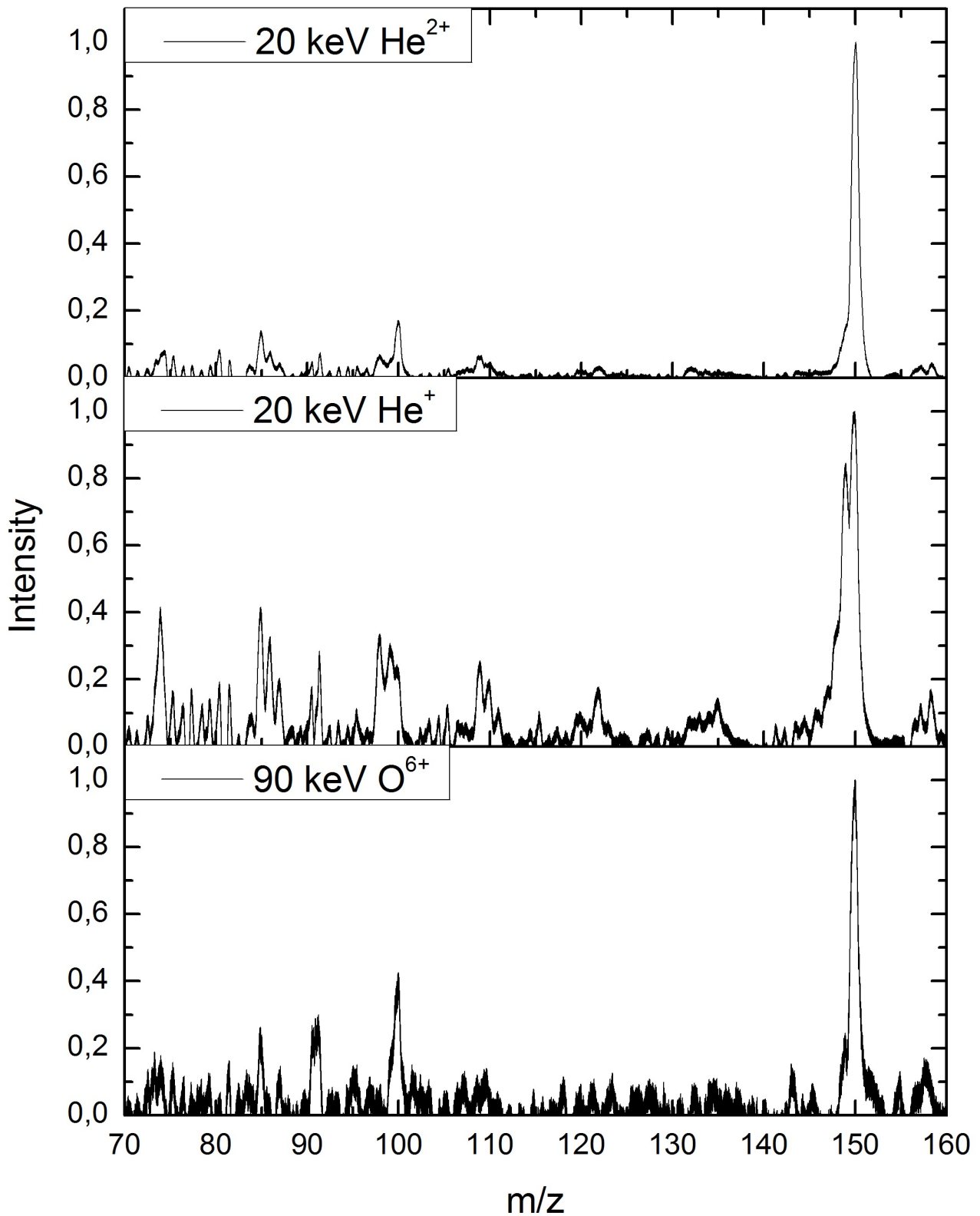


Figure 24: Three coronene fragment mass spectra resulting from three different ions of similar velocity, normalized to the coronene dication peak at $m/z=150$.

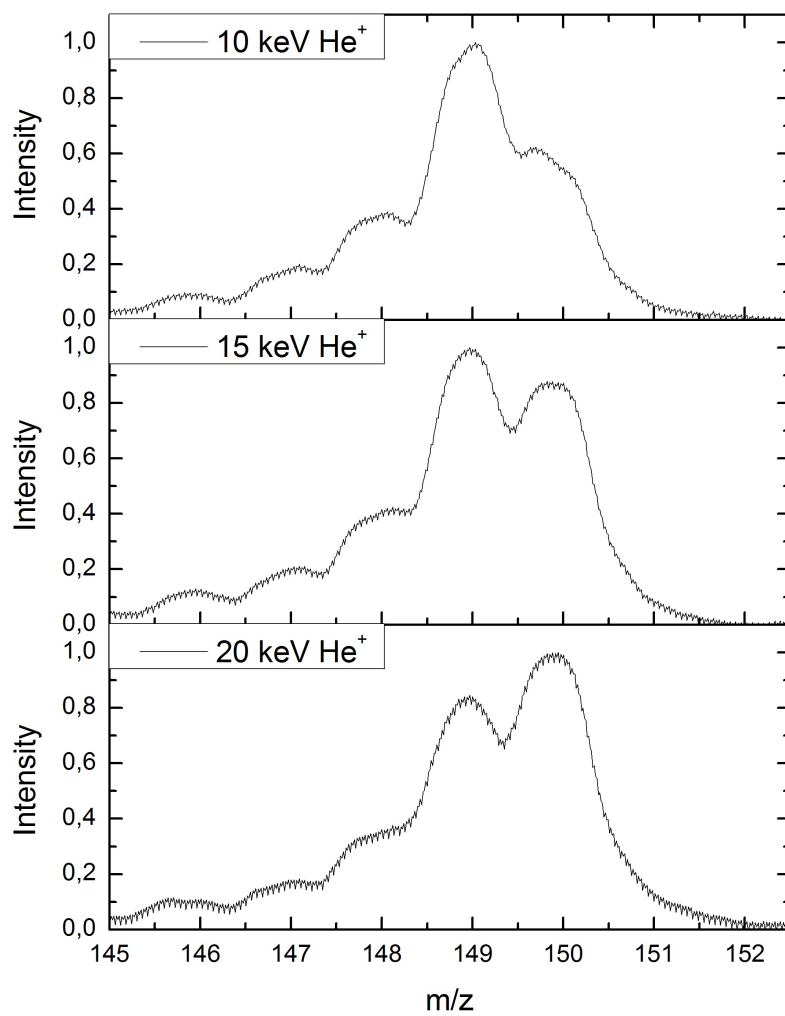


Figure 25: The coronene dication and its hydrogen loss peaks for He⁺ ions colliding on coronene⁺. The hydrogen loss peaks are decreasing for an increasing kinetic energy.

4 Conclusion

In this thesis, absolute cross sections are obtained for interaction of ions on coronene for different ions and for different kinetic energies of these ions. There is no energy-dependence of the cross sections in the energy range up to the energy corresponding to the classical orbital velocity of the coronene electrons. The average value of cross sections and their fitting standard deviations for H^+ , He^+ and He^{2+} are $6.5 \pm 0.4 \cdot 10^{-15} \text{ cm}^2$, $6.5 \pm 0.9 \cdot 10^{-15} \text{ cm}^2$ and $10.9 \pm 0.5 \cdot 10^{-15} \text{ cm}^2$ respectively. The cross sections for O^{5+} and O^{6+} are found to be $7.7 \pm 0.2 \cdot 10^{-15} \text{ cm}^2$ and $9.9 \pm 0.2 \cdot 10^{-15} \text{ cm}^2$ respectively, but the accuracy of those measurements is doubted. The cross sections for He^+ and H^+ are similar, so there is no ion-dependence. There is a dependence on the charge of the ion; the cross sections for the helium ions and the protons are lower than both the predictions of the OVB-model and the predictions of the model of Forsberg et al., but they have a similar dependence on the charge state. The used method is a good method to get a rough estimate (a standard deviation of $\sim 10\%$) of the cross section, but is insufficient for a more precise determination.

5 Acknowledgements

I would like to thank Geert, Thomas and Ronnie for their help and supervision and Steven for reviewing this thesis. I also would like to thank the other group members: Dmitri, Edita, Erwin, Jan, Leon and Olmo. I am also grateful for the technical assistance of the werkplaats, electronics and the tekenkamer.

References

- [1] C. Bosetti, P. Boffetta & C. La Vecchia (2007) *Annals of Oncology* **18**, 431-446
- [2] Wolfgang Wilcke (2007) *Geoderma* **141**, 157-166
- [3] A.G.G.M. Tielens (2008) *Annual Review of Astronomy and Astrophysics* **46**, 289-337
- [4] E.R. Micelotta, A.P. Jones & A.G.G.M. Tielens (2010) *Astronomy & Astrophysics* **510**, A36
- [5] Max P. Bernstein, Scott A. Sandford, Louis J. Allamandola, J. Seb Gillette, Simon J. Clemett, Richard N. Zare (1999) *Science* **283**, 1135-1138
- [6] G. Reitsma, H. Zettergren, L. Boschman, E. Bodewits, R. Hoekstra & T. Schlathölter (2013) *Journal of Physics B* **46**, 245201
- [7] Alexander von Zastrow, Rico Otto, Sébastien Jézouin, Jonathan Brox, Martin Stei, Olmo González-Magaña, Geert Reitsma, Thomas Schlathölter, Ronnie Hoekstra, Thorsten Best & Roland Wester (2014) *Applied Physics B* **114**, 251-255
- [8] A. Lawicki, A.I.S. Holm, P. Rousseau, M. Capron, R. Maisonnny, S. Maclot, F. Seitz, H.A.B Johansson, S. Rosén, H.T. Schmidt, H. Zettergren, B. Manil, L. Adoui, H. Cederquist & B.A. Huber (2011) *Physical Review A* **83**, 022704
- [9] S. Denifl, B. Sonnweber, J. Mack, L.T. Scott, P. Scheier, K. Becker & T.D. Märk (2006) *International Journal of Mass Spectrometry* **249-250**, 353-358
- [10] Steven Knoop (2006), PhD-thesis
- [11] Lecture notes RUG-course *Atomic and Molecular Interactions* (2013)
- [12] B.O. Forsberg, J.D. Alexander, T. Chen, A.T. Pettersson, M. Gatchell et al. (2013) *The Journal of Chemical Physics* **138**, 054306
- [13] <http://www.fysik.su.se/henning/models/>
- [14] Sadia Bari (2010), PhD-thesis
- [15] Olmo González-Magaña (2013), PhD-thesis
- [16] Meike Door (2011), Ma-thesis
- [17] Simon J. Gaskell (1997) *Journal of Mass Spectrometry*, **32**, 677-688
- [18] John B. Fenn (2003), Nobel Lecture
- [19] Geoffrey Taylor (1964) *Proceedings of the Royal Society of London. Series A, Mathematical and Physical Sciences* **280**, No. 1382, 383-397
- [20] Paul Kebarle & Udo H. Verkerk (2009) *Mass Spectrometry Reviews* **28**, 898-917
- [21] Ryan R. Julian, Sarah R. Mabbett & Martin F. Jarrold (2005) *Journal of American Society of Mass Spectrometry* **16**, 1708-1712
- [22] W. Paul (1990) *Review of Modern Physics* **62**, 531
- [23] D. Douglas & J. French (1992) *Journal of American Society of Mass Spectrometry* **3**, 398

- [24] Joseph Ladislav Wiza (1979) *Nuclear Instruments and Methods* **162**, 587-601
- [25] David A. Dahl *SIMION 3D 8.0*, Idaho National Engineering and Environmental Laboratory
- [26] H.W. Jochims, E. Rühl, H. Baumgärtel, S. Tobita and S. Leach (1994) *Astrophysical Journal* **420**, 307-317

A Settings

Setup settings:

V_{needle}	3.75-5.23 kV
Flow rate	0.16 ml/h
$V_{capillary}$	100 V
$V_{funnel\ entrance}$	130 V
$V_{funnel\ exit}$	26 V
Power funnel	44 W/50 Ohm
Frequency RF funnel	195 kHz
$V_{diaphr.}$	22 V
Power 1 st quadrupole	148 W/50 Ohm
Frequency RF 1 st quadrupole	834.5 kHz
$V_{RF-4pl\ bias}$	7.8 V
V_{p1}	6 V
V_{p2}	-5 V
$V_{ESI-pulse}$	50 V
$V_{einzl\ lens}$	7.3 V
$V_{pp\ trap}$	2000 V
$V_{faraday\ cup}$	-100 V
V_{L1}	-100 V
V_{L2}	-2400 V
$V_{float\ detector}$	-3000 V
$V_{MCP\ in\ detector}$	-5000 V
$V_{MCP\ out\ detector}$	-3000 V
$V_{TOF\ cage}$	-3000 V

Mass filter settings:

Mass	303
Offset voltage	2.4 V
Low mass (ΔM)	1003
High mass (ΔRes)	330

Pulse settings:

	Delay	Width	Scan
Extraction pulse	0 s	0.001 s	1,2
ESI trapping	0.05 s	0.05 s	1,2
Buffer gas	0.05 s	0.05 s	1,2
Ion beam	0.20 s	0.025 - 9.75 s	2

B Cross section fits & Mass spectra

This appendix contains the cross section fits and their fitting errors, their date of experiment and the beam current during the experiment. The last three figures are the mass spectra of He^+ , He^{2+} and O^{6+} .

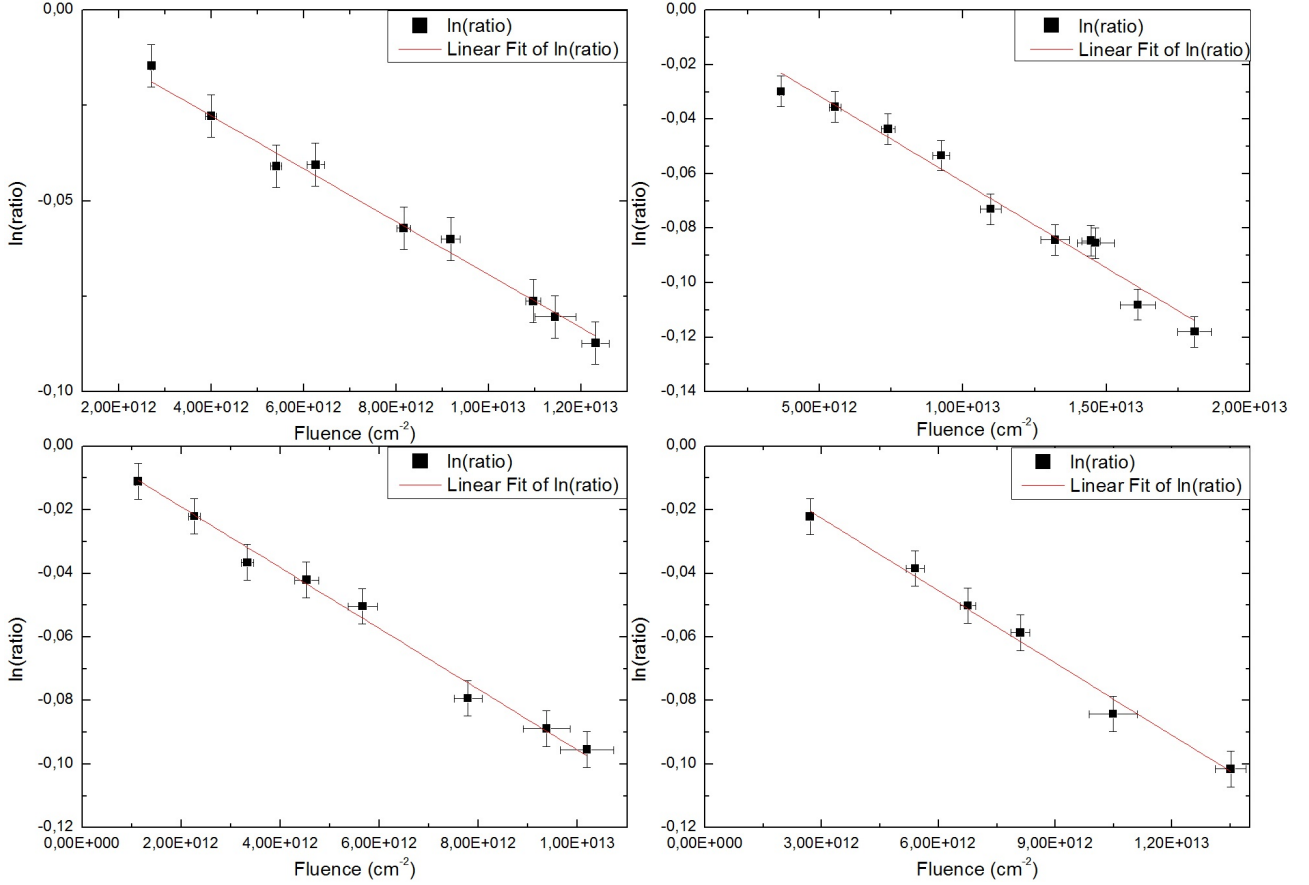


Figure 26: The fits for four cross sections.

Upper left: 7.5 keV H^+ ; $6.93 \cdot 10^{-15} \pm 1.03 \cdot 10^{-16}$, 23-01-2014, ~ 67 nA

Upper right: 10 keV H^+ ; $6.31 \cdot 10^{-15} \pm 1.35 \cdot 10^{-16}$, 23-01-2014, ~ 90 nA

Bottom left: 12.5 keV H^+ ; $9.56 \cdot 10^{-15} \pm 1.72 \cdot 10^{-16}$, 15-01-2014, ~ 28 nA

Bottom right: 15 keV H^+ ; $7.58 \cdot 10^{-15} \pm 1.37 \cdot 10^{-16}$, 23-01-2014, ~ 33 nA

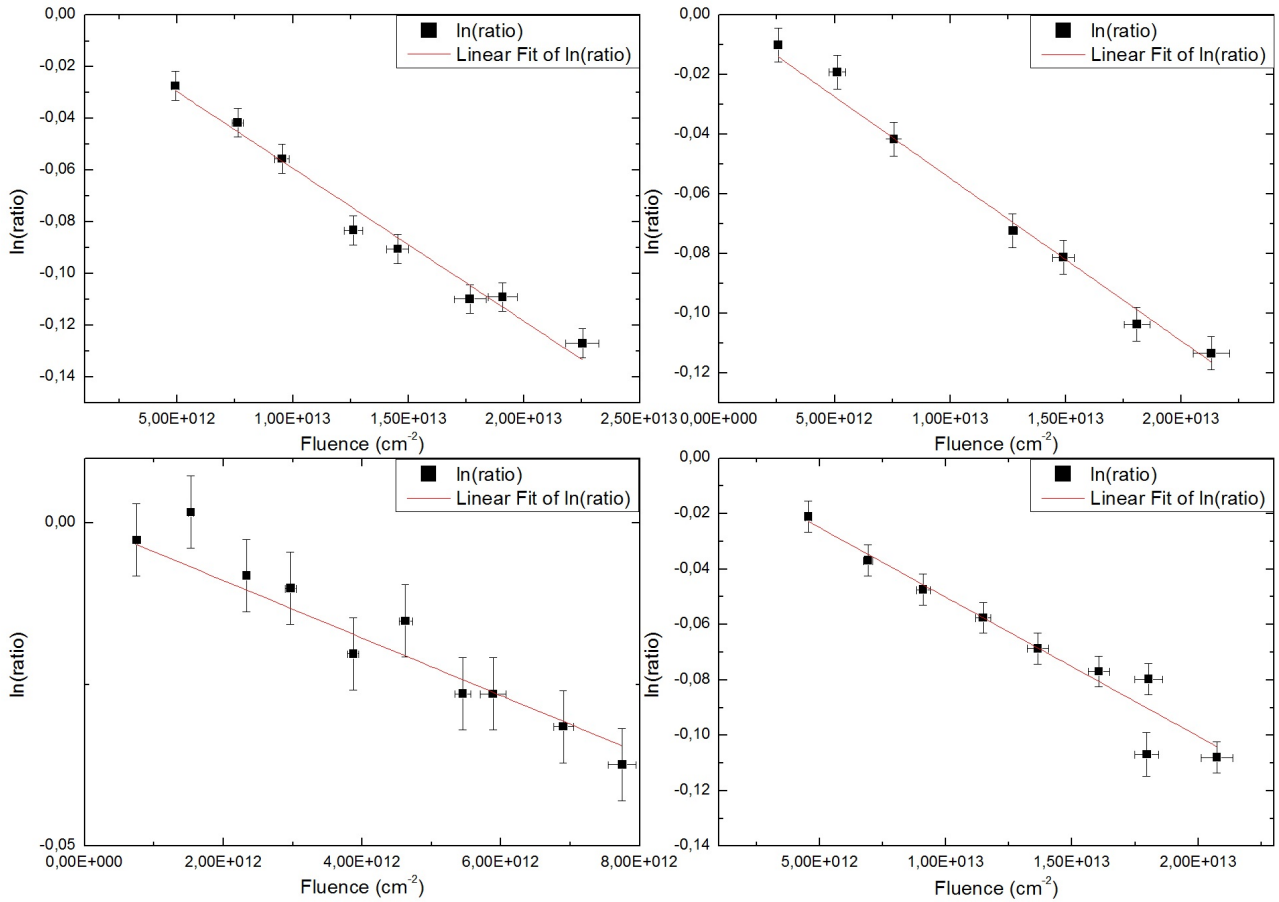


Figure 27: The fits for four cross sections.

Upper left: 17.5 keV H⁺; $5.92 \cdot 10^{-15} \pm 1.26 \cdot 10^{-16}$, 20-01-2014, ~ 60 nA

Upper right: 20 keV H⁺; $5.47 \cdot 10^{-15} \pm 1.34 \cdot 10^{-16}$, 20-01-2014, ~ 63 nA

Bottom left: 22.5 keV H⁺; $4.45 \cdot 10^{-15} \pm 2.62 \cdot 10^{-16}$, 17-01-2014, ~ 10 nA

Bottom right: 25 keV H⁺; $5.02 \cdot 10^{-15} \pm 1.51 \cdot 10^{-16}$, 20-01-2014, ~ 114 nA

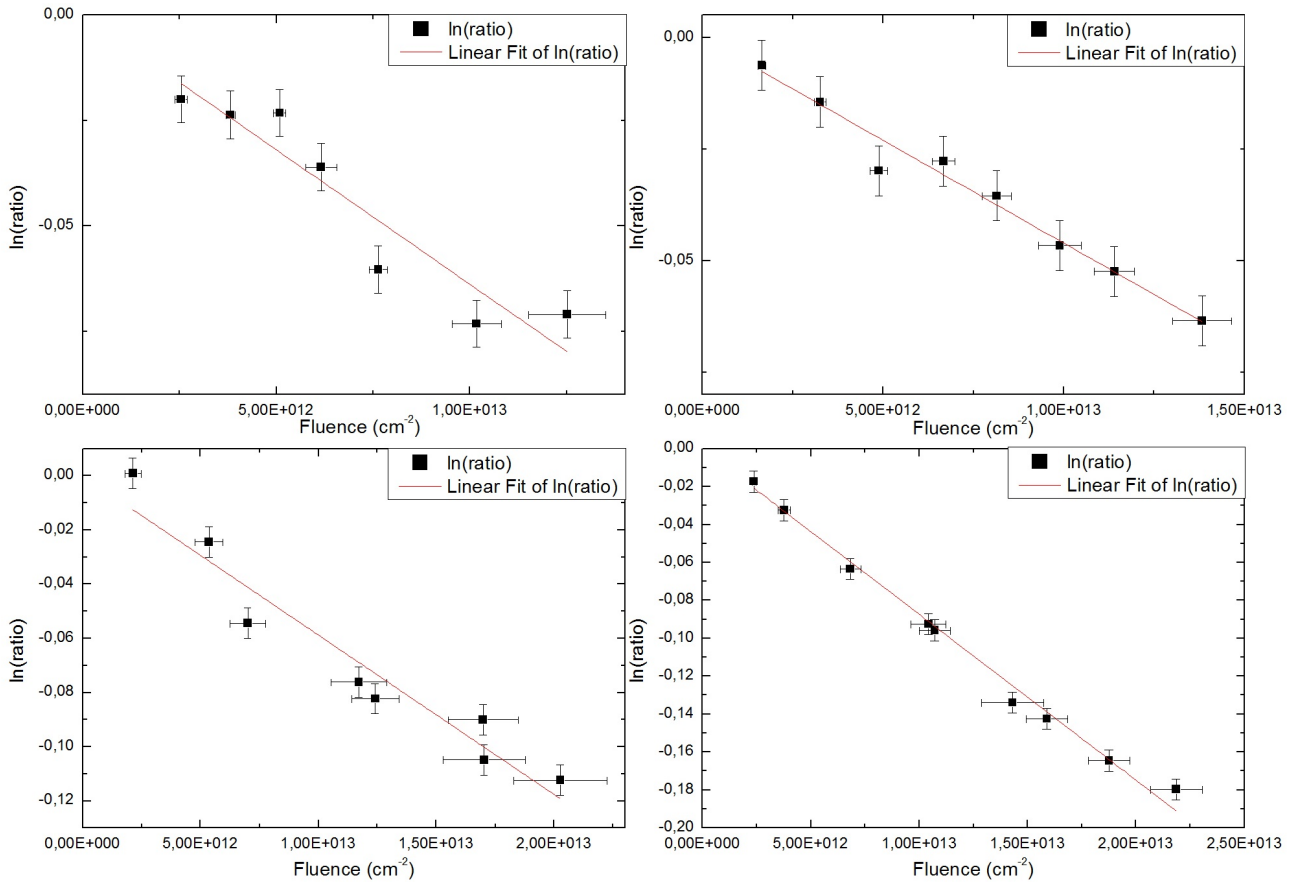


Figure 28: The fits for four cross sections.

Upper left: 10 keV He^+ ; $6.39 \cdot 10^{-15} \pm 4.04 \cdot 10^{-16}$, 14-01-2014, ~ 30 nA

Upper right: 14 keV He^+ ; $4.61 \cdot 10^{-15} \pm 1.33 \cdot 10^{-16}$, 15-01-2014, ~ 42 nA

Bottom left: 17.5 keV He^+ ; $5.88 \cdot 10^{-15} \pm 2.72 \cdot 10^{-16}$, 14-01-2014, ~ 150 nA

Bottom right: 20 keV He^+ ; $8.74 \cdot 10^{-15} \pm 1.42 \cdot 10^{-16}$, 13-01-2014, ~ 250 -300 nA

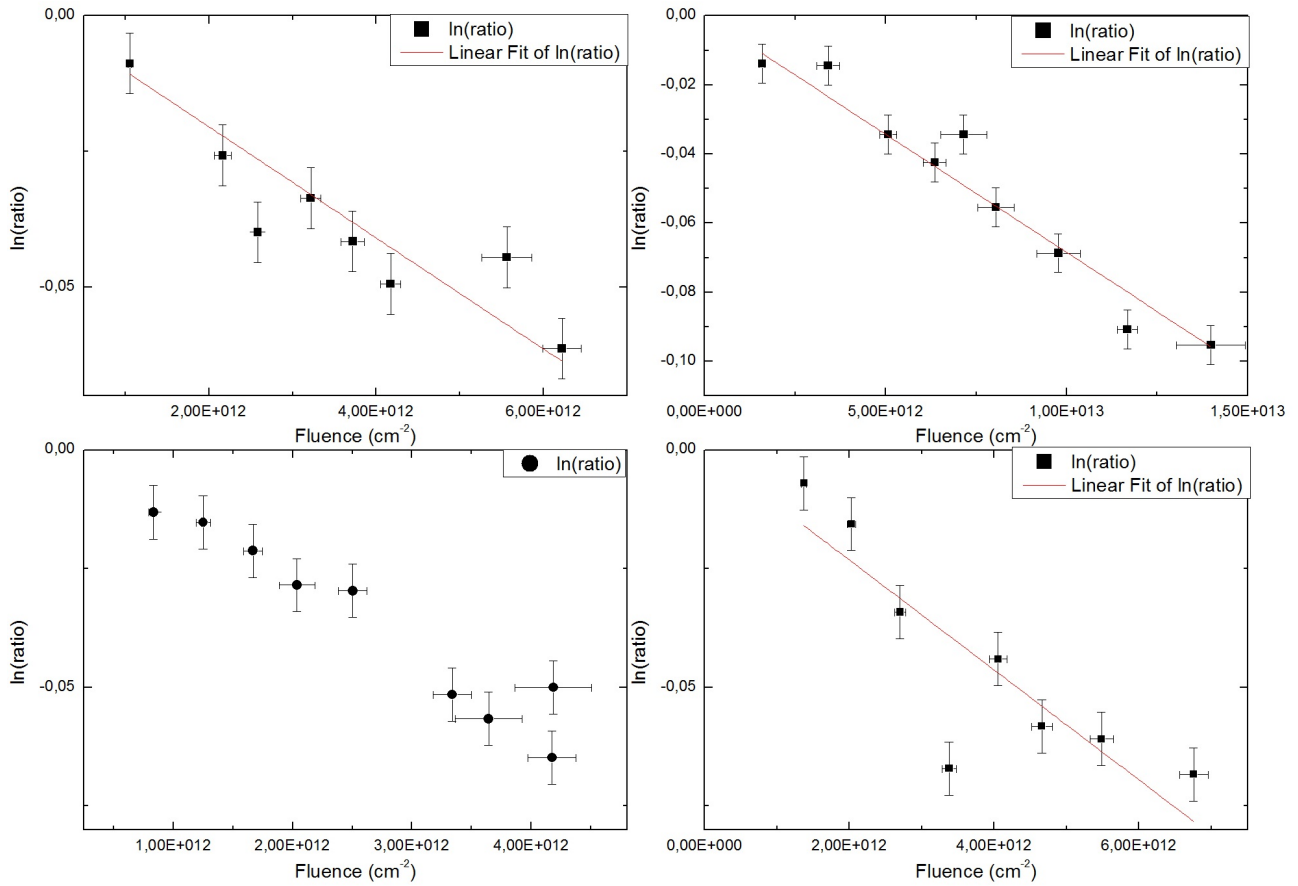


Figure 29: The fits for four cross sections.

Upper left: 25 keV He⁺; $6.85 \cdot 10^{-15} \pm 2.91 \cdot 10^{-16}$, 15-01-2014, ~ 46 nA

Upper right: 20 keV He²⁺; $1.02 \cdot 10^{-14} \pm 6.93 \cdot 10^{-16}$, 14-01-2014, ~ 60 nA

Bottom left: 25 keV He²⁺; $1.41 \cdot 10^{-14} \pm 5.90 \cdot 10^{-16}$, 14-01-2014, ~ 21 nA

Bottom right: 30 keV He²⁺; $1.16 \cdot 10^{-14} \pm 1.05 \cdot 10^{-15}$, 13-01-2014, ~ 68 nA

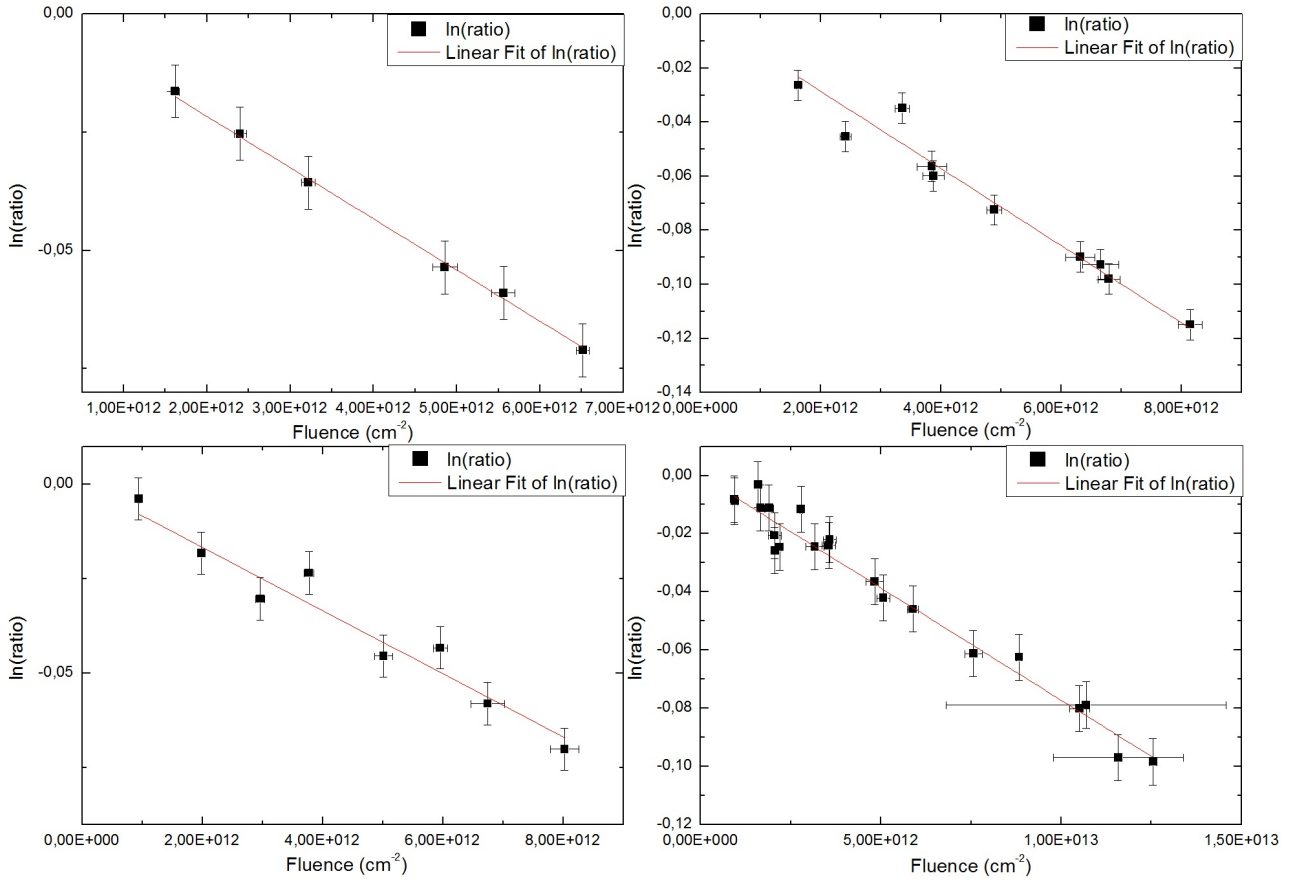


Figure 30: The fits for four cross sections.

Upper left: 35 keV He^{2+} ; $1.08 \cdot 10^{-14} \pm 9.62 \cdot 10^{-17}$, 14-01-2014, ~ 80 nA

Upper right: 40 keV He^{2+} ; $1.43 \cdot 10^{-14} \pm 3.72 \cdot 10^{-16}$, 13-01-2014, ~ 85 nA

Bottom left: 50 keV He^{2+} ; $8.34 \cdot 10^{-15} \pm 3.61 \cdot 10^{-16}$, 15-01-2014, ~ 100 nA

Bottom right: 75 keV O^{5+} ; $7.72 \cdot 10^{-15} \pm 1.85 \cdot 10^{-16}$, 04-02-2014 & 05-02-2014, ~ 14 nA

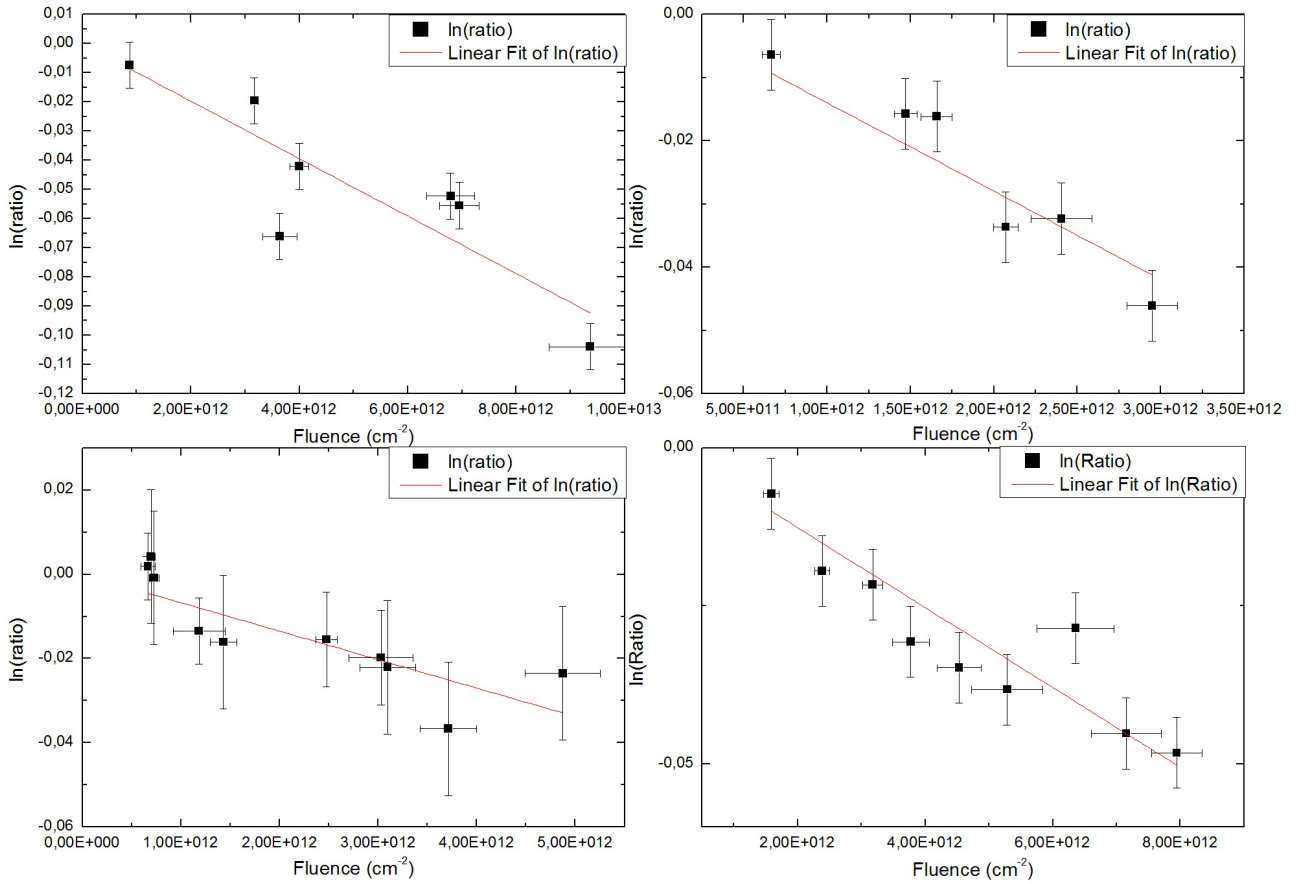


Figure 31: The fits for four cross sections.

Upper left: 72 keV O⁶⁺; $9.58 \cdot 10^{-15} \pm 1.09 \cdot 10^{-15}$, 06-02-2014, ~ 10 nA

Upper right: 108 keV O⁶⁺; $1.40 \cdot 10^{-14} \pm 1.03 \cdot 10^{-15}$, 24-01-2014, ~ 8 nA

Bottom left: 150 keV O⁶⁺; $6.76 \cdot 10^{-15} \pm 9.03 \cdot 10^{-16}$, 03-02-2014, ~ 6 nA

Bottom right: 15 keV H⁺; $6.32 \cdot 10^{-15} \pm 3.83 \cdot 10^{-16}$, 16-01-2014, ~ 30 nA

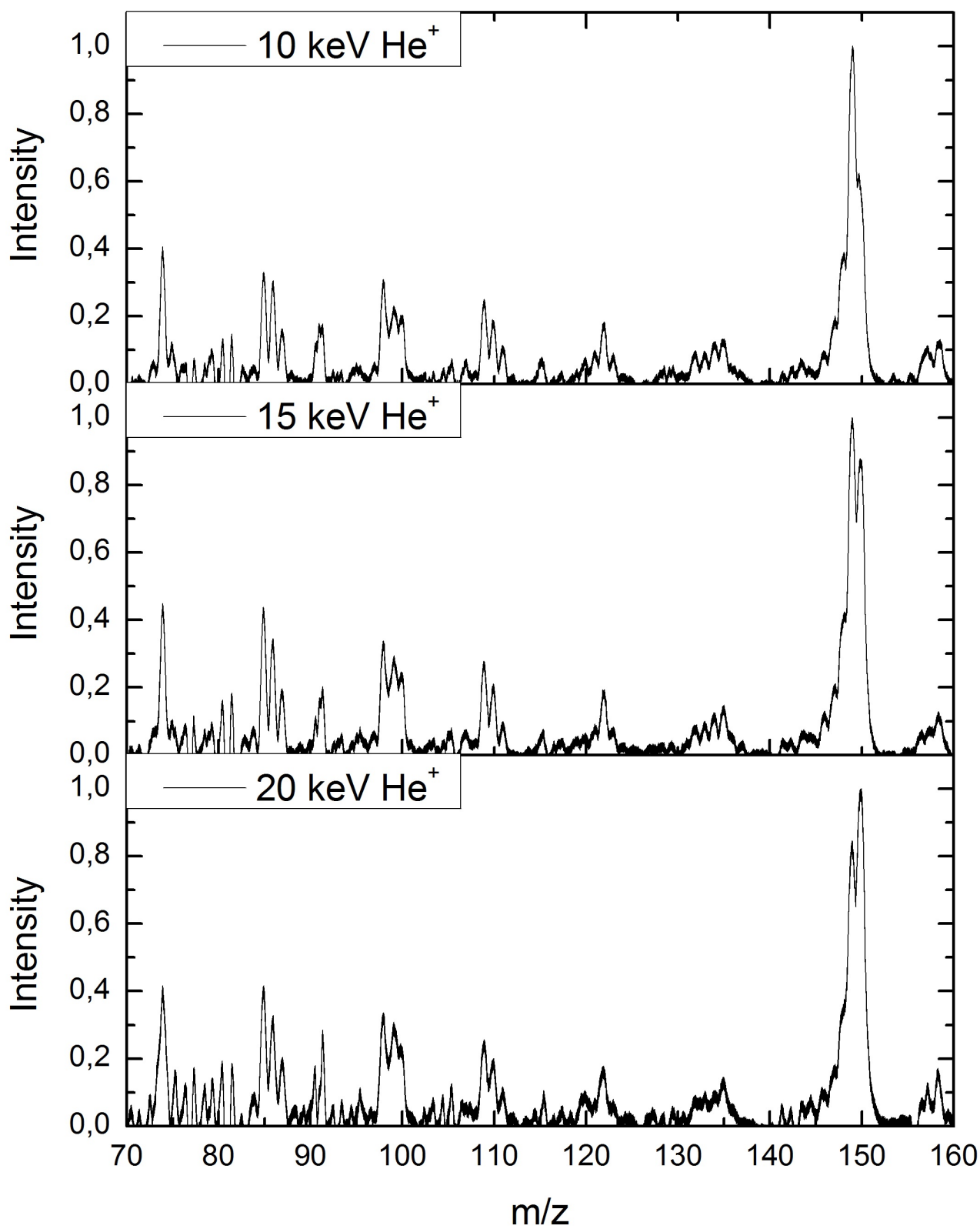


Figure 32: The coronene fragment mass spectra resulting from collisions with He⁺ ions.

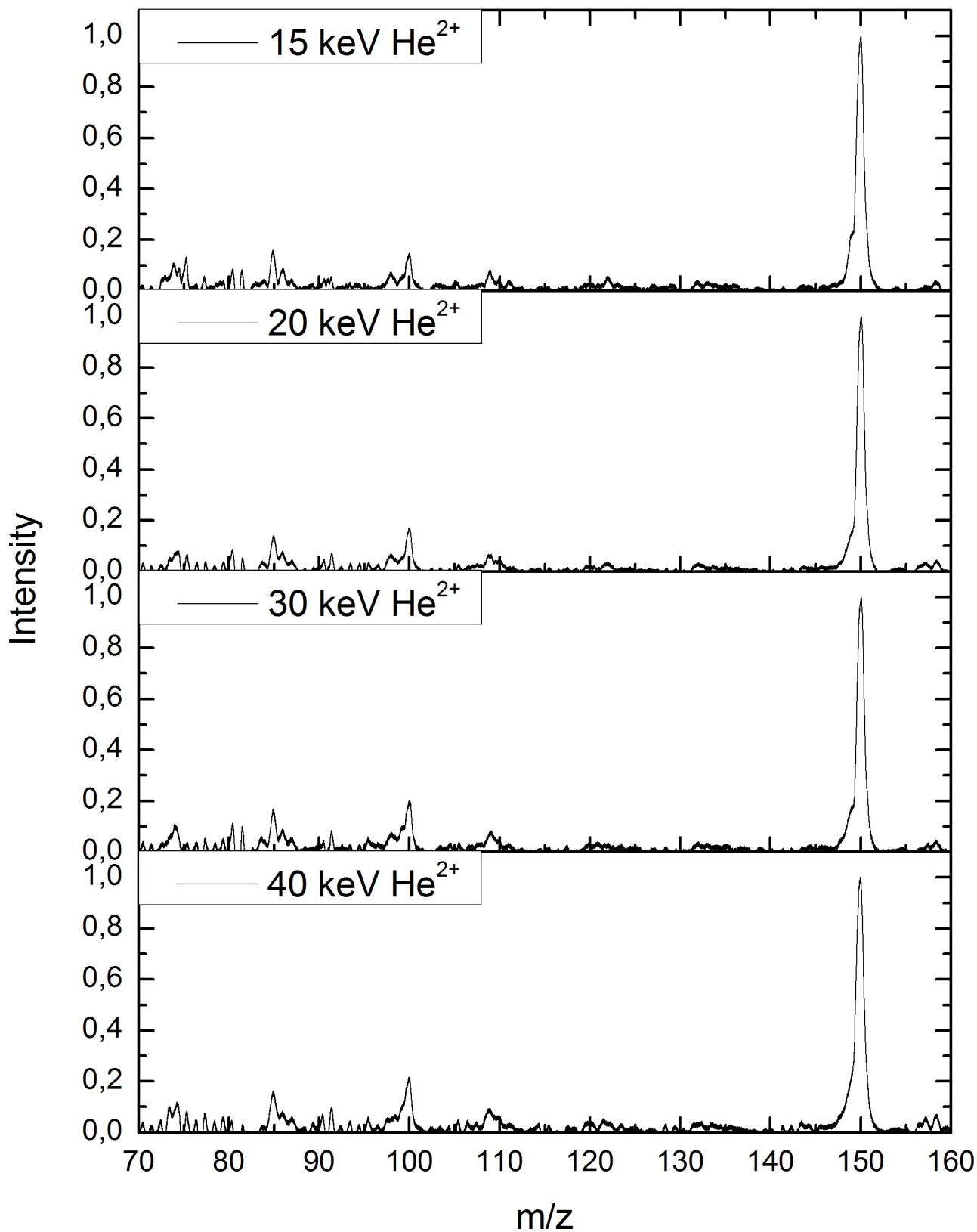


Figure 33: The coronene fragment mass spectra resulting from collisions with He²⁺ ions.

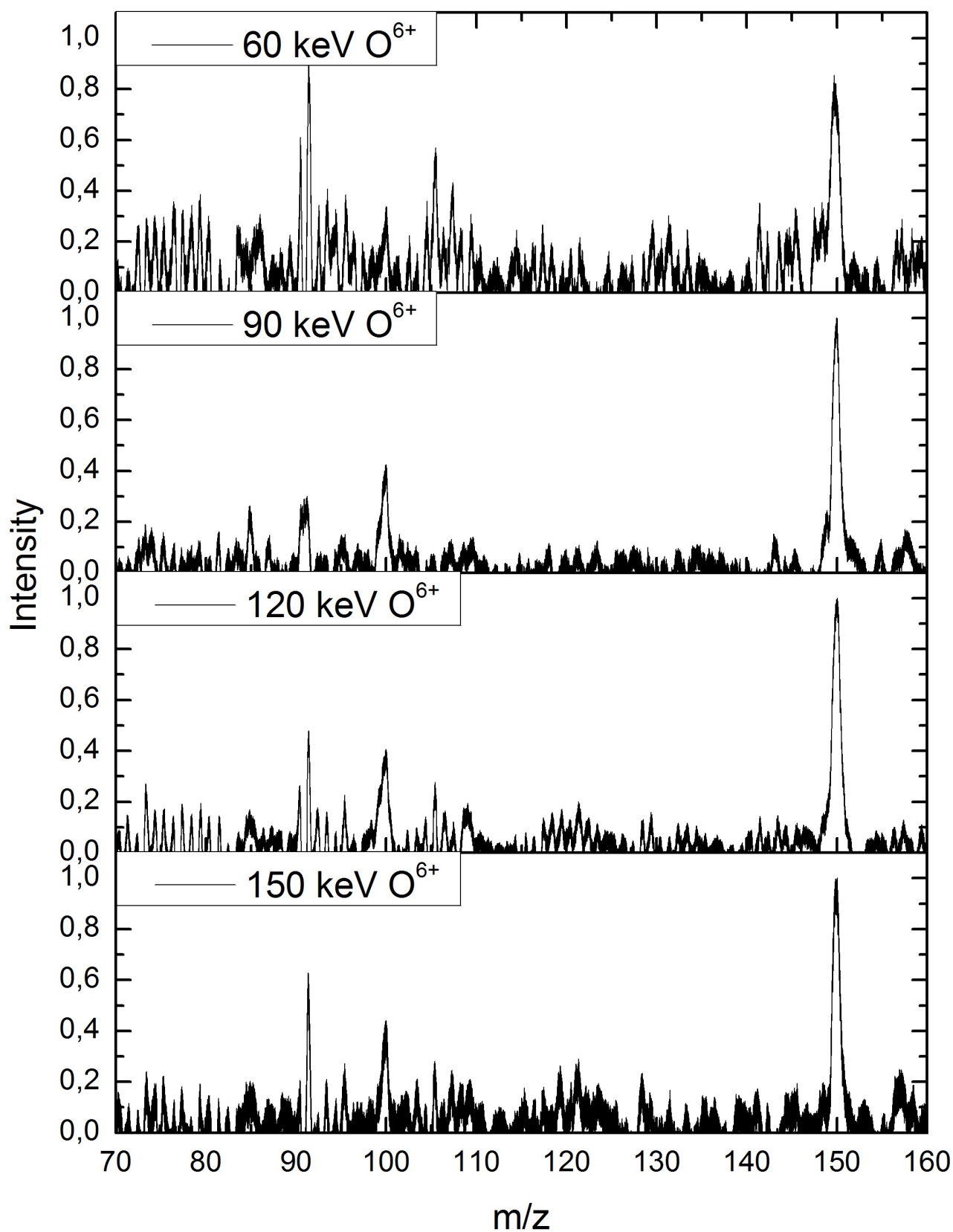


Figure 34: The coronene fragment mass spectra resulting from collisions with O^{6+} ions.